Autonomous Navigation for Binary Asteroid Landing

Elffers, P.A.; Caroselli, Edoardo; van Kampen, E.; Mooij, E.

DOI
10.2514/6.2024-0322

Publication date
2024

Document Version
Final published version

Published in
Proceedings of the AIAA SCITECH 2024 Forum

AIAA SciTech Forum
8-12 January 2024, Orlando, FL
AIAA SCITECH 2024 Forum

10.2514/6.2024-0322

Autonomous Navigation for Binary Asteroid Landing

Peter Elffers* and Edoardo Caroselli†
Airbus Defence & Space, 88090 Immenstaad am Bodensee, Germany

Erik-Jan van Kampen‡ and Erwin Mooij§
Delft University of Technology, 2629 HS Delft, The Netherlands

This paper investigates the performance of an autonomous navigation system to navigate a spacecraft in the proximity of a binary asteroid system using optical and laser ranging measurements. The knowledge about the binary asteroid is limited to its orbital parameters and ellipsoid shape models. The accelerometer bias random walk is included in the estimation process. Over a four-hour landing maneuver starting from 6770 m altitude and ending at 550 m, the mean position estimation uncertainty is 41.6 m (3σ). It is shown that the navigation accuracy is sensitive to the Sun phase angle, the irregularity of the asteroid shape, and the goodness of fit of the ellipsoid shape model. The paper demonstrates that the navigation system is robust to large errors in the initialization of the extended Kalman filter state. The impact of image distortion and two types of image noise on the navigation performance are investigated.

I. Introduction

Asteroids are gaining widespread attention from space agencies and industry because of their uniquely preserved environment since the formation of the Solar System, their potential for rare materials mining, and planetary defence purposes. Several missions dedicated to small bodies have been successfully launched and completed. In 2001, NASA's NEAR became the first spacecraft to orbit and land on an asteroid [1]. In 2010, JAXA successfully returned samples of the asteroid (25143) Itokawa with its Hayabusa-1 spacecraft [2], and ESA's Rosetta mission put a lander on the comet 67P/Churyumov-Gerasimenko in 2014 [3].

Because of the interest in asteroid exploration, many researchers have studied and developed navigation systems to safely operate spacecraft in the vicinity of asteroids. For proximity operations in missions that involve landings, autonomous navigation is required because of signal delays that come with Earth-based navigation. Typically, the spacecraft combines optical measurements from cameras [4] and laser rangers [5] to estimate its position relative to the asteroid. The spacecraft attitude is determined using star trackers and rate gyros [6].

The images from navigation cameras can produce various measurements such as the line of sight (LOS) [7, 8], centroid and apparent diameter (CAD) [9, 10], and landmark tracking [4, 11, 12]. The type of measurement depends on the altitude and the camera field of view (FOV), with landmarks becoming smaller in the images as the altitude increases. In general, camera measurements suffer from range ambiguity. CAD attempts to mitigate this issue by using a-priori knowledge about the size and shape of the asteroid and its projection onto the camera sensor. The lack of an accurate shape model combined with difficult lighting conditions makes it very difficult to estimate the radial range from optical measurements. If multiple bodies can be observed by the camera(s), triangulation techniques can be used to provide range measurements [13, 14]. A formation of spacecraft can solve the range ambiguity problem with cameras alone, if interspacecraft measurements are available [15]. A common solution to solve the range ambiguity problem for a single spacecraft is to use a Light Detection and Ranging (lidar) or laser range finders (LRFs) in combination with the navigation cameras [8, 16].

Gil-Fernández (2018) shows that a spacecraft can autonomously navigate in a binary asteroid environment by solely observing the primary asteroid [17]. However, this requires augmenting the state vector with the gravitational parameter of the asteroid and the pointing error resulting from varying illumination conditions. Dietrich (2014) demonstrates that given an ellipsoid shape model for the asteroid, LRFs alone can be used to navigate the spacecraft [5]. They show that

*MSc. Student, Airbus Defence & Space, TESOA-1, p.a.elffers@gmail.com.
†PhD Student, Airbus Defence & Space, TESOA-1, edoardo.caroselli@airbus.com.
‡Assistant Professor, Faculty of Aerospace Engineering, Section Control and Simulation, e.vankampen@tudelft.nl.
§Associate Professor, Faculty of Aerospace Engineering, Section Astrodynamics and Space Missions, e.mooij@tudelft.nl. Associate Fellow AIAA.

using more than three LRFs does not benefit the state estimation anymore, which is attributed to the geometry and symmetric nature of the ellipsoid surface. Takahashi (2021) proposes a navigation solution that is tightly coupled to the guidance algorithm, in the sense that impulsive ΔV maneuvers issued by the guidance are subsequently measured by onboard accelerometers [18]. Integration of the accelerometer data then yields information about the spacecraft position change over time.

This paper investigates a navigation solution for a binary asteroid system that exploits measurements of both asteroids in the camera frame, similar to [13], combined with a single LRF measurement that uses ellipsoid models for the asteroids in a manner similar to that in [5]. The navigation camera will provide LOS measurements, which are corrected for varying illumination conditions as is done in [17]. The intended use of the navigation solution is at medium to far distances because the LOS cannot be determined at very close distance when an asteroid fills the entire field of view of the camera. The contribution of this paper is a navigation filter that leverages the binary nature of the asteroid system in combination with a LRF. This navigation filter is robust to filter state initialization errors due to the high observability with both asteroids in sight, in combination with the LRF. Contrary to the landmark-based approaches, this approach only requires an ellipsoid shape model to determine the position relative to the asteroid.

This navigation system is developed in the framework of the NEO-MAPP study*, which uses ESA's Hera mission as a reference. The goal is to land a μLander on Dimorphos, the smallest asteroid of the binary system (65803) Didymos [19]. This μLander is detached from the Hera mothership at an altitude of around 5 km and navigates autonomously. The landing site for the μLander is a predefined point on the surface of Dimorphos. The spacecraft must therefore know its position in the asteroid reference frame. The requirement for the position knowledge is that the 3σ uncertainty in the position is less than 10% of the altitude. To save time and money, there will not be an early characterization phase in which a database of landmarks is collected along with a precise shape model, as is common practise in asteroid landing missions [2, 12]. A separate navigation system is developed for the final phase of the landing [20, 21]. Throughout the paper, the attitude control system is assumed to be a separate system, providing perfect pointing in the desired direction.

The paper is structured as follows: Sec. II gives an overview of the binary asteroid dynamics. Section III presents the onboard sensors, their mathematical models, and how they are used in the navigation system. The Extended Kalman Filter (EKF) development is described in Sec. IV, followed by an analysis and discussion of simulation results in Sec. V. The conclusions of the research and recommendations for future work are given in Sec. VI. Finally, in Appendix A the mathematics behind the LRF measurement model are described, and Appendix B shows a verification test for the LRF measurement model.

II. Dynamics

The dynamic environment around binary asteroids is one of the most complex environments found in the Solar System. This is due to the irregular shape and composition of the asteroids, combined with third-body perturbations, solar radiation pressure (SRP) and often short rotation periods. This section describes the modeling of the binary asteroid environment and its dynamics.

A. Target binary asteroid

Didymos consists of two asteroids named Didymos (primary) and Dimorphos (secondary). Throughout the paper, the naming of primary and secondary will be used. The asteroid characteristics, including ellipsoid shape models, are given in [22]. This description of Didymos is valid for its state before the impact of DART on 26 September 2023†. A summary of the most relevant parameters of Didymos is given in Table 1. The secondary asteroid is tidally locked with the primary.

B. Reference frames

Four reference frames are used in this work: inertial, primary, secondary, and body. These frames are denoted by $\mathcal{F}_{\mathcal{I}}$, $\mathcal{F}_{\mathcal{P}}$, $\mathcal{F}_{\mathcal{S}}$, and $\mathcal{F}_{\mathcal{B}}$, respectively, and are shown in Fig. 1. The inertial frame is a modified J2000 frame, whose origin is in the binary system's barycenter. The axes of the inertial frame are aligned with the J2000 frame, meaning that the Z-axis points in the direction of the Earth mean rotation pole at epoch J2000, the X-axis points toward the mean equinox at epoch J2000, and the Y-axis completes the right-handed coordinate system. The primary and secondary reference frame have their origins in the centers of mass of the respective asteroids. Their Z-axes point in the direction

*`https://neomapp.eu/abstract/`, last accessed 2023/03/11

†`https://www.nasaspaceflight.com/2022/09/dart-impact/`, last accessed 2023/03/13

Table 1 Main characteristics of binary asteroid Didymos [22].

Property	Nominal value	Uncertainty (1σ)
Diameter of primary	780 m	±30 m
Diameter of secondary	164 m	±18 m
Density of primary	2170 kg/m^3	±350 kg/m^3
Orbit radius of secondary	1.19 km	±0.03 km
Total mass of system	5.278e11 kg	±0.54e11 kg
Rotation period of primary	2.2600 h	±0.0001 h
Secondary orbital period	11.9217 h	±0.0002 h
Spin pole of primary	Parallel to secondary orbital spin pole	

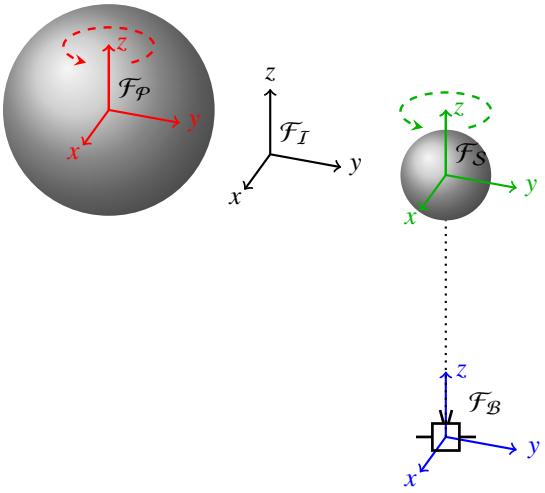

Fig. 1 Sketch of the four reference frames used in this paper. Dimensions are not to scale. Orientation of the asteroids is chosen arbitrarily.

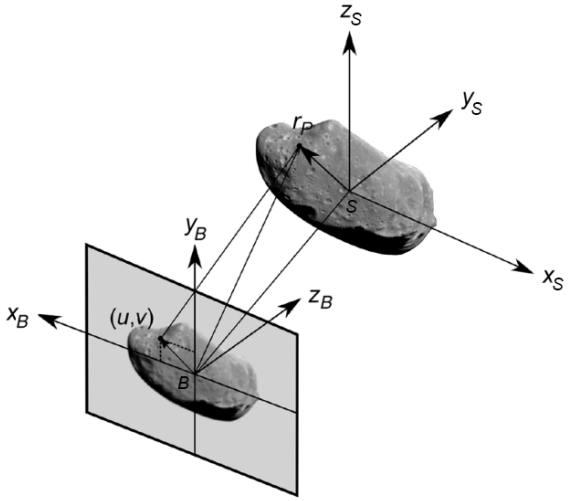

Fig. 2 Projection of a point P defined in the $\mathcal{F}_\mathcal{S}$ frame onto the camera sensor in the $\mathcal{F}_\mathcal{B}$ frame. Adapted from [8].

of maximum moment of inertia, their X-axes in the direction of minimum moment of inertia, and their Y-axes complete the right-handed coordinate systems. The asteroids rotate around their Z-axes. The body frame is fixed to the spacecraft, with the Z-axis aligned with the camera line of sight, and the X- and Y-axes aligned with the camera sensor as shown in Fig. 2. The camera frame is assumed to coincide and align with the body frame and is therefore not mentioned separately. The LRF points along the Z-axis of $\mathcal{F}_\mathcal{B}$, and is assumed to coincide with the origin of $\mathcal{F}_\mathcal{B}$. The vector notation used in this paper is as follows: $\boldsymbol{r}_I^{SB}$ is a position vector from the origin of $\mathcal{F}_\mathcal{S}$ to the origin of $\mathcal{F}_\mathcal{B}$, defined in $\mathcal{F}_\mathcal{I}$. $\boldsymbol{R}_{IB}$ is a direction cosine matrix that transforms a vector from $\mathcal{F}_\mathcal{B}$ to $\mathcal{F}_\mathcal{I}$.

C. Spacecraft translational dynamics

The translational dynamics are described in the $\mathcal{F}_\mathcal{I}$ frame. The equations of motion are written as:

$$\dot{\boldsymbol{r}}_I^{IB} = \boldsymbol{v}_I^{IB} \tag{1}$$

$$\dot{\boldsymbol{v}}_I^{IB} = \boldsymbol{g}_I + \boldsymbol{a}_{\text{ext}} \tag{2}$$

where $\boldsymbol{r}$ is the position vector, $\boldsymbol{v}$ the velocity vector, $\boldsymbol{g}$ the gravity vector, and $\boldsymbol{a}_{\text{ext}}$ the external acceleration vector from sources other than gravity. The gravity and external acceleration vector will be examined in more detail.

1. Gravity field

The gravity field around asteroids is often highly irregular and as a result a point mass gravity model does not suffice. The spherical harmonics gravity model is a popular choice to precisely model a body's gravity field [23], however its convergence is limited to the body's circumscribing sphere [24]. The spherical harmonics model is therefore not suitable to simulate trajectories that reach within the circumscribing sphere, which is not an unlikely scenario when landing on an asteroid's surface. Alternatively, the polyhedron gravity model can be used to transform a 3D polyhedron model into a gravity model, assuming a constant density [25]. The polyhedron gravity $\boldsymbol{g}_{\text{ast}}$, defined in the asteroid reference frame, is a summation over the edges and faces of the 3D polyhedron model:

$$\boldsymbol{g}_{\text{ast}} = \nabla U = -G\rho \sum_{e \in \text{edges}} \boldsymbol{E}_e \boldsymbol{r}_e L_e + G\rho \sum_{f \in \text{faces}} \boldsymbol{F}_f \boldsymbol{r}_f \omega_f \tag{3}$$

In this equation, U is the gravity potential, G is the gravitation constant, ρ is the mean density of the asteroid, $\boldsymbol{E_e}$ is a dyadic matrix of an edge, $\boldsymbol{r}_e$ and $\boldsymbol{r}_f$ are the distances from a point to an edge and a face, L_e is a dimensionless per-edge factor, $\boldsymbol{F}_f$ is an outer product of a face normal with itself, and ω_f is a dimensionless per-face factor.

For the 3D polyhedron models of the primary and secondary, modified versions of the asteroids Bennu and Itokawa are used. Their respective shape models have been determined during the OSIRIS-REx and Hayabusa-1 missions [26, 27]. This decision is motivated by the desire to have a simulated reality in the camera simulator that is more realistic than the ellipsoid shape models given in [22]. This comes with the benefit of testing the robustness of the developed algorithms on realistic shape models.

The 3D polyhedron models of Bennu and Itokawa are stretched to match the extent of the ellipsoid models along their principal axes of inertia. After calculating the volume of the reshaped 3D polyhedron models, the density of the two asteroids is recalculated to match the mass of the reshaped asteroids to the masses given in [22].

Third-body perturbations are neglected, as for altitudes below 5 km they are orders of magnitude smaller than the other accelerations such as that due to SRP, control acceleration, and gravitational pull.

2. External accelerations

The external accelerations that are simulated consist of the SRP and the guidance acceleration. The SRP due to the albedo of the asteroids is neglected. The constrained terminal velocity guidance algorithm is used to calculate the desired guidance acceleration [28]. The propulsion system dynamics are not considered, thus the calculated guidance acceleration is directly applied to a point mass model of the spacecraft.

A cannonball model is used to model the SRP. The cannonball model considers the spacecraft to be a sphere and as a result the attitude of the spacecraft is not part of the SRP calculation. An analysis on the impact of assuming a cannonball SRP model on the spacecraft dynamics in the vicinity of a binary asteroid environment is given in [29]. The acceleration due to SRP, perpendicular to the Sun direction, can be calculated as follows [30]:

$$\frac{m a_{\text{srp}}}{A_\perp} = \rho p_{\text{sun}} \tag{4}$$

where

$$p_{\text{sun}} = \frac{E}{c} = p_0 \left(\frac{r_\oplus}{r} \right)^2 \tag{5}$$

with

$\rho = 1.2$	[-]	assumed surface reflectivity
$c = 2.99792458 \times 10^8$	[m/s]	speed of light
$E = (1372 \pm 45)\left(\frac{r_\oplus}{r}\right)^2$	[W/m^2]	intensity of solar radiation (seasonal)
$p_0 = (4.58 \pm 0.15) \times 10^{-6}$	[N/m^2]	solar radiation pressure at 1 au (seasonal)
$r_\oplus = 1.4962 \times 10^8$	[km]	mean radius of Earth's orbit
$A_\perp = 1$	[m^2]	surface area of the spacecraft projected in the Sun direction

D. Spacecraft rotational dynamics

The rotational dynamics of the spacecraft are not modeled. The pointing knowledge of the spacecraft is assumed to be supplied by the GNC subsystem through a conventional star tracker and rate gyro setup. No pointing errors are taken

into account.

E. Asteroid translational and rotational dynamics

The orbit of the asteroids and the Sun are modeled using the Hera SPICE kernels[‡]. The position and orientation of the Solar System bodies is returned in the J2000 reference frame.

III. Onboard sensors

The spacecraft is equipped with various onboard sensors essential for its operation. The characteristics of these sensors and how they are modeled is described here in more detail. The star trackers and gyros are not considered in this section because the attitude control and determination problem is assumed to be solved by a separate spacecraft subsystem. The remaining sensors are the accelerometers, the LRF, and the navigation camera.

A. Accelerometers

The accelerometers measure the proper acceleration of the spacecraft. The accelerometers are assumed to be perfectly aligned with the three axes of the $\mathcal{F}_\mathcal{B}$ frame. The accelerometer measurements $\boldsymbol{a}_{\text{meas},B}$ are subject to noise and bias random walk:

$$\boldsymbol{a}_{\text{meas},B}(t) = \boldsymbol{a}_B(t) + \boldsymbol{b}_{\text{acc},B}(t) + \boldsymbol{\eta}_{\text{acc}}(t) \tag{6}$$

where $\boldsymbol{b}_{\text{acc},B}$ is the bias random walk:

$$\dot{\boldsymbol{b}}_{\text{acc},B}(t) = \boldsymbol{\eta}_{\text{acc,bias}}(t) \tag{7}$$

In Eqs. (6) and (7), $\boldsymbol{\eta}_{\text{acc}}$ and $\boldsymbol{\eta}_{\text{acc,bias}}$ are zero-mean white noise vectors with standard deviations of 2.8284×10^{-4} m/s^2 and 2.8284×10^{-5} m/s^3, respectively. These values are conform the specifications of the accelerometers chosen by Airbus for the NEO-MAPP μLander.

B. Navigation camera

The navigation camera is used in combination with image processing to detect the location of the asteroid centroid in the image. Using this centroid location and a camera model, a unit vector towards the asteroid is calculated in the $\mathcal{F}_\mathcal{B}$ frame. The process is visualized in Fig. 2, where a point P on the asteroid is projected onto the camera sensor, yielding the pixel coordinates (u,v). A unit vector in the direction of P, defined in the $\mathcal{F}_\mathcal{B}$ frame, is then calculated using a camera model. This unit vector contains information about the relative direction of the asteroid with respect to the spacecraft, which can be used in the navigation filter.

1. Camera characteristics

The characteristics of the camera are given in Table 2. A virtual scene with the two asteroids is created in the Planet and Asteroid Natural Scene Generation Utility[§] (PANGU) [31]. The 3D models used for the asteroids are reshaped versions of Bennu and Itokawa, as explained in subsubsection II.C.1. PANGU runs inside of the MATLAB/Simulink® simulator. The inputs for PANGU are the Sun position, asteroids positions and orientations, and the spacecraft position and orientation. Two example images that are rendered in PANGU are shown in Figs. 3 and 4.

2. Camera model

A camera model is used to extract spatial information from the images. An example is given in Fig. 2, where a point P is projected onto the camera sensor. The inverse is also possible: given the pixel coordinates (u,v), a unit direction vector can be calculated. All points in the direction of this vector project to the pixel coordinates (u,v). The pinhole camera model [32] is used to calculate the pixel coordinates associated with the projection of a point P defined in $\mathcal{F}_\mathcal{B}$:

$$\begin{pmatrix} u \\ v \end{pmatrix} = \frac{f}{h_{\text{px}} Z_B^{BP}} \begin{pmatrix} X_B^{BP} \\ Y_B^{BP} \end{pmatrix} \tag{8}$$

[‡] `http://spiftp.esac.esa.int/data/SPICE/hera/misc/hera.html`, last accessed 2023/03/13

[§] `https://pangu.software/`, last accessed 2023/03/15

Table 2 Characteristics of the navigation camera

Property	Value
Resolution	512x512 px
Focal length f	50 mm
Field of view	30°
Pixel size h_{px}	0.052×10^{-3} m/px
Pixel angular size h_{cam}	0.0010 rad/px

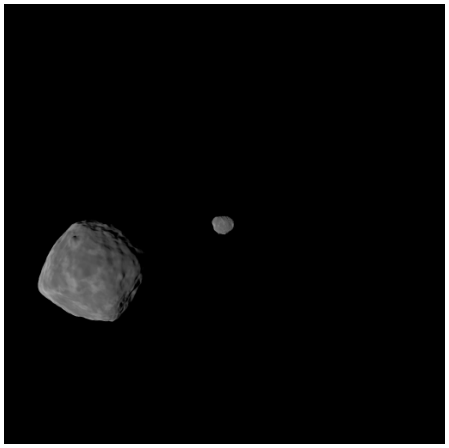

Fig. 3 Navigation camera output at 6500 m distance from the surface of the secondary. Own work, rendered in PANGU.

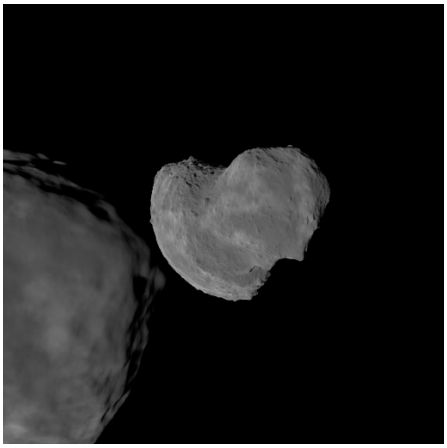

Fig. 4 Navigation camera output at 500 m distance from the surface of the secondary. Own work, rendered in PANGU.

3. Image processing

The camera images are processed to extract the centroid locations of the asteroids in pixel coordinates. These centroids are then used as measurements in the navigation filter. The centroid extraction procedure is challenging due to varying illumination conditions, overlapping asteroids, asteroids that are (partially) out of the image, and irregular shapes. Furthermore, the centroids must be assigned the correct label 'primary' or 'secondary'. In the framework of the image processing, two terms are defined:

Center of figure (cof): the projection of the center of mass (com) of the asteroid onto the camera sensor, in pixel coordinates.

Center of brightness (cob): the centroid of a region of pixels that is detected in the image, in pixel coordinates.

The motion of the center of mass of the asteroids is described in the SPICE kernels. Therefore, ideally we measure the center of figure, as this gives the direction towards a known point in inertial space. However, due to varying lighting conditions casting shadows on the asteroid surface, and irregular asteroid shapes, this is not possible. For example, in Fig. 3 the larger asteroid has a shadow region on the right side, which moves the center of brightness location to the left relative to the center of figure. To mitigate this discrepancy between the center of figure and center of brightness, [17] proposes a factor $\boldsymbol{\varepsilon}_{\text{cob}}$ that corrects for the changing illumination conditions by shifting the center of brightness in the direction opposite of the Sun direction in the camera frame. The definition of the correction factor and the subsequent correction to obtain an estimate for the center of figure are given by[¶]:

$$\boldsymbol{\varepsilon}_{\text{cob}} = \arctan\left(\frac{8\pi R}{3r}\sin^2\left(\frac{\phi}{2}\right)\right)\frac{\boldsymbol{u}_{\text{det}}}{h_{\text{cam}}} \tag{9}$$

$$\hat{\boldsymbol{p}}_{\text{cof}} = \boldsymbol{\varepsilon}_{\text{cob}} + \boldsymbol{p}_{\text{cob}} \tag{10}$$

[¶]Private communication with Jesus Gil-Fernandez, the author of [17], resulted in a slightly modified equation for $\boldsymbol{\varepsilon}_{\text{cob}}$ than what is written in his paper. Date: 2022/12/01

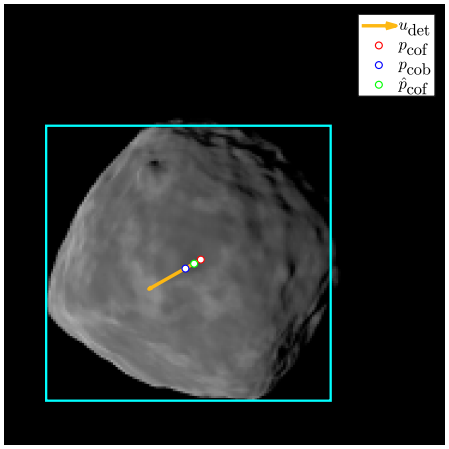

Fig. 5 Key concepts from the image processing. Note that p_{cob} is shifted in the direction opposite of u_{det} to obtain $\hat{p}_{\text{cof}}$.

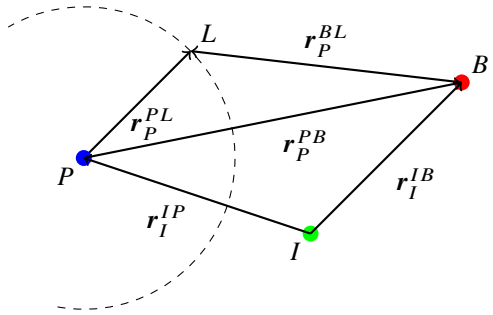

Fig. 6 Sketch of the LRF beam r_P^{BL} intersecting the surface of asteroid P in the point L. Also shown are the position of P and B in the I-frame.

with

$\boldsymbol{\varepsilon}_{\text{cob}}$	[px]	lighting conditions correction factor
$\hat{\boldsymbol{p}}_{\text{cof}}$	[px]	estimated center of figure pixel coordinates
$\boldsymbol{p}_{\text{cob}}$	[px]	center of brightness pixel coordinates
R	[m]	mean radius of asteroid
r	[m]	spacecraft position norm in asteroid-fixed reference frame
ϕ	[rad]	Sun phase angle
$\boldsymbol{u}_{\text{det}}$	[m]	unit vector of Sun direction in camera sensor plane
$h_{\text{cam}} = 0.0010$	[rad/px]	pixel angular size

The correction procedure is visualized in Fig. 5. A limitation of $\boldsymbol{\varepsilon}_{\text{cob}}$ is that in its derivation, a spherical shape is assumed. Therefore, the correction will be less effective or even harm the estimation of $\hat{\boldsymbol{p}}_{\text{cof}}$ if the asteroid shape is non-spherical. For this reason, the correction is only applied to the primary asteroid, but not to the secondary asteroid. All steps of the image processing algorithm are given in Algorithm 1.

Algorithm 1 Image processing

1: Convert the image to grayscale.
2: Binarize the image. Every grayscale pixel is converted to either 1 (white) or 0 (black). The threshold that determines to which group a pixel belongs is set using Otsu's method [33].
3: Fill holes in the image. A hole is defined as a set of background pixels that cannot be reached by filling in the background from the edge of the image.
4: Extract the area, centroid location, and bounding box of each 8-connected object in the binary image.
5: Assign the label 'primary' or 'secondary' to each detected object based on the minimum distance between the object centroid and the predicted projection of the primary and secondary center of mass.
6: Sort the objects within the primary and secondary lists by their area. Select the largest two objects from each list.
7: Apply the Sun phase angle correction $\boldsymbol{\varepsilon}_{\text{cob}}$ to the largest object corresponding to the primary asteroid.
8: Discard the objects if their bounding boxes overlap each other. Stop simulation.
9: Discard objects if their bounding box touches the edges of the frame.
10: Discard all measurements if the distance between two consecutive $\hat{\boldsymbol{p}}_{\text{cof}}$ is beyond a threshold value.

The output of the image processing is either one or two sets of pixel coordinates that represent a center of figure, or a zero output. The logic that determines the subsequent steps, which ultimately leads to exploiting the measurement to gain knowledge about the system state, is included in the navigation filter.

C. Laser range finder

The LRF points in the same direction as the camera, the Z-axis of $\mathcal{F}_{\mathcal{B}}$, and provides a distance measurement to a point on the surface of the asteroid. The distance r_{LRF} measured by the LRF between the spacecraft and a point L on the surface of the primary asteroid is sketched in Fig. 6 and is expressed as:

$$r_{\text{LRF}} = \left\| \boldsymbol{r}_P^{PL} - \boldsymbol{r}_P^{PB} \right\| \tag{11}$$

The measurement is obtained using PANGU and uses the reshaped 3D models of Bennu and Itokawa. If there would be a pointing error, this is directly reflected in the measurement from PANGU.

IV. Extended Kalman Filter development

This section presents the navigation concept that is implemented using an EKF, the EKF state vector, and the propagation and measurement update steps of the EKF. Directly following the EKF development is a description of the reference landing scenario, the initial setup and tuning of the EKF, and the verification and validation procedure for the simulator and the EKF.

A. Navigation concept

The navigation concept is to autonomously navigate in the binary asteroid environment by combining prior knowledge with onboard measurements. The prior knowledge consists of the ellipsoid shape models, point mass gravity fields, the ephemeris of the asteroids given by the SPICE kernels, and spacecraft parameters. The onboard measurements are obtained by the accelerometers, the camera, and the laser range finder. The camera and laser range finder yield measurements that are relative to the asteroids. Using the ephemeris and (known) attitude, these measurements can be used to estimate the position and velocity of the spacecraft in inertial space. Measurements of both asteroids are used to exploit the binary nature of the asteroid system to provide a better state estimate.

B. State vector definition

The camera and LRF measurements can be relative to both the primary and the secondary asteroid. The camera can provide two measurements, one to each asteroid, if both asteroids are in the image. It is favorable to define the position and velocity in the state vector in the $\mathcal{F}_{\mathcal{I}}$ frame because measurements from both the primary and secondary asteroid can be easily transformed into the $\mathcal{F}_{\mathcal{I}}$ frame through the SPICE kernel ephemeris. The state vector consists of the position and velocity of the spacecraft in the $\mathcal{F}_{\mathcal{I}}$ frame, and the accelerometer bias random walk in the $\mathcal{F}_{\mathcal{B}}$ frame, as defined in Eqs. (6) and (7). The bias random walk $\boldsymbol{b}_{\text{acc},B}$ is also called the accelerometer bias. The state vector is thus as follows:

$$\boldsymbol{x} = \begin{pmatrix} \boldsymbol{r}_I^{IB} & \dot{\boldsymbol{r}}_I^{IB} & \boldsymbol{b}_{\text{acc},B} \end{pmatrix}^T = \begin{pmatrix} r_{I,x}^{IB} & r_{I,y}^{IB} & r_{I,z}^{IB} & \dot{r}_{I,x}^{IB} & \dot{r}_{I,y}^{IB} & \dot{r}_{I,z}^{IB} & b_{\text{acc},B,x} & b_{\text{acc},B,y} & b_{\text{acc},B,z} \end{pmatrix}^T \tag{12}$$

C. Propagation

The true inertial acceleration of the spacecraft is unknown. Therefore, the measured acceleration, corrected for the accelerometer bias, is used in the filter. The uncertainty in this measurement is included in the propagation equation through the $\boldsymbol{G}$ matrix and the input noise vector $\boldsymbol{\omega}$. Point mass gravity models are used to lower the complexity of the model that is run onboard of the spacecraft. The nonlinear propagation equation is as follows:

$$\dot{\boldsymbol{x}} = f(\boldsymbol{x}, \boldsymbol{u}) + \boldsymbol{G}\boldsymbol{\omega} = \begin{pmatrix} \dot{\boldsymbol{r}}_I^{IB} \\ \ddot{\boldsymbol{r}}_I^{IB} \\ \dot{\boldsymbol{b}}_{\text{acc},B} \end{pmatrix} + \boldsymbol{G} \begin{pmatrix} \boldsymbol{\eta}_{\text{acc}} \\ \boldsymbol{\eta}_{\text{acc,bias}} \end{pmatrix} =$$

$$\begin{pmatrix} \dot{\boldsymbol{r}}_I^{IB} \\ -\mu_p \dfrac{\boldsymbol{r}_I^{IB} - \boldsymbol{r}_I^{IP}}{|\boldsymbol{r}_I^{IB} - \boldsymbol{r}_I^{IP}|^3} - \mu_s \dfrac{\boldsymbol{r}_I^{IB} - \boldsymbol{r}_I^{IS}}{|\boldsymbol{r}_I^{IB} - \boldsymbol{r}_I^{IS}|^3} + \boldsymbol{R}_{IB}(\boldsymbol{a}_{\text{meas},B} - \boldsymbol{b}_{\text{acc},B}) \\ \boldsymbol{0}_{3x1} \end{pmatrix} + \begin{bmatrix} \boldsymbol{0}_{3x3} & \boldsymbol{0}_{3x3} \\ -\boldsymbol{R}_{IB} & \boldsymbol{0}_{3x3} \\ \boldsymbol{0}_{3x3} & \boldsymbol{I}_{3x3} \end{bmatrix} \begin{pmatrix} \boldsymbol{\eta}_{\text{acc}} \\ \boldsymbol{\eta}_{\text{acc,bias}} \end{pmatrix} \tag{13}$$

To propagate the state estimation error covariance matrix $\boldsymbol{P}$ of the EKF, the Jacobian of the state derivative is used. It is given by Eq. (14). The term $\frac{\partial \ddot{\boldsymbol{r}}_I^{IB}}{\partial \boldsymbol{r}_I^{IB}}$ is the gravity gradient and is found in [34].

$$\boldsymbol{F}_x = \frac{\partial f(\boldsymbol{x},\boldsymbol{u})}{\partial \boldsymbol{x}} = \frac{\partial}{\partial \boldsymbol{x}} \begin{pmatrix} \dot{\boldsymbol{r}}_I^{IB} \\ -\mu_p \frac{\boldsymbol{r}_I^{IB} - \boldsymbol{r}_I^{IP}}{|\boldsymbol{r}_I^{IB} - \boldsymbol{r}_I^{IP}|^3} - \mu_s \frac{\boldsymbol{r}_I^{IB} - \boldsymbol{r}_I^{IS}}{|\boldsymbol{r}_I^{IB} - \boldsymbol{r}_I^{IS}|^3} + \boldsymbol{R}_{IB}(\boldsymbol{a}_{\text{meas},B} - \boldsymbol{b}_{\text{acc},B}) \\ \boldsymbol{0}_{3x1} \end{pmatrix} = \begin{bmatrix} \boldsymbol{0}_{3x3} & \boldsymbol{I}_{3x3} & \boldsymbol{0}_{3x3} \\ \frac{\partial \ddot{\boldsymbol{r}}_I^{IB}}{\partial \boldsymbol{r}_I^{IB}} & \boldsymbol{0}_{3x3} & -\boldsymbol{R}_{IB} \\ \boldsymbol{0}_{3x3} & \boldsymbol{0}_{3x3} & \boldsymbol{0}_{3x3} \end{bmatrix} \tag{14}$$

Finally, the process noise covariance matrix $\boldsymbol{Q}$ is created using the accelerometer noise and bias covariances:

$$\boldsymbol{Q} = \begin{bmatrix} \boldsymbol{\sigma}^2_{\text{acc}} & \boldsymbol{0}_{3x3} \\ \boldsymbol{0}_{3x3} & \boldsymbol{\sigma}^2_{\text{acc,bias}} \end{bmatrix} \tag{15}$$

D. Measurement update

The measurement update step includes the Kalman gain calculation, the measurement update itself, and the update of the state estimation error covariance matrix $\boldsymbol{P}$. An essential part in these calculations is the function $z = h(\boldsymbol{x}, \boldsymbol{u})$, which calculates the measurement z that corresponds to the state $\boldsymbol{x}$ and input $\boldsymbol{u}$. The Jacobian of $h(\boldsymbol{x}, \boldsymbol{u})$, called $\boldsymbol{H}_x$, is used in the Kalman gain calculation and in the update of $\boldsymbol{P}$. The measurements that must be calculated are the pixel coordinates of the expected center of figures of the asteroids, and the expected distance to the asteroid surface measured by the LRF. The measurement updates for the camera and LRF are performed separate from one another. Details on the measurement update for the camera and the LRF are given below.

1. Camera update

For every image that the camera outputs, the image processing determines how many asteroids are in the image. If no asteroids are found, no measurement update is executed. If one or two asteroids are found, z will be of size 2x1 or 4x1. In the following, it is assumed that only the primary asteroid is detected by the image processing.

The image processing outputs $\hat{\boldsymbol{p}}_{\text{cof}}$, the estimated center of figure of the primary asteroid in pixel coordinates. To calculate the measurement that is expected given the current state estimate $\hat{\boldsymbol{x}}_{\text{filter}}$, $z = h(\boldsymbol{x}, \boldsymbol{u})$ is used. The knowledge of the ephemeris of the asteroid through its SPICE kernel, which gives the center of mass location of the primary asteroid in $\mathcal{F}_{\mathcal{I}}$, is used in the calculation of $z = h(\boldsymbol{x}, \boldsymbol{u})$ as well. This center of mass location must now be projected onto the camera sensor as shown in Fig. 2. First, it must be transformed into the $\mathcal{F}_{\mathcal{B}}$ frame. This is done as follows:

$$\boldsymbol{r}_B^{BP} = \boldsymbol{R}_{BI}(\boldsymbol{r}_I^{IP} - \boldsymbol{r}_I^{IB}) \tag{16}$$

where $\boldsymbol{R}_{BI}$ and $\boldsymbol{r}_I^{IP}$ are given by the SPICE kernel, and $\boldsymbol{r}_I^{IB}$ is part of $\hat{\boldsymbol{x}}_{\text{filter}}$. The next step is to use the pinhole camera model, Eq. (8), to calculate the pixel coordinates corresponding to the projection of $\boldsymbol{r}_B^{BP}$ onto the camera sensor. The coordinates are shifted by 256 pixels to transform them to the image coordinate system, because in the image coordinate system (0,0) is at the image border while in the pinhole model it is at the center of the image. The resulting equation is:

$$z = h(\boldsymbol{x}, \boldsymbol{u}) = \boldsymbol{p}_{\text{cof}} = \frac{f}{h_{\text{px}} Z_B^{BP}} \begin{pmatrix} X_B^{BP} \\ Y_B^{BP} \end{pmatrix} + \begin{pmatrix} 256 \text{ px} \\ 256 \text{ px} \end{pmatrix} \tag{17}$$

Now to find $\boldsymbol{H}_x$, the Jacobian of $h(\boldsymbol{x}, \boldsymbol{u})$ is calculated:

$$\boldsymbol{H}_x = \frac{\partial h(\boldsymbol{x},\boldsymbol{u})}{\partial \boldsymbol{x}} = \begin{bmatrix} \frac{\partial h(\boldsymbol{x},\boldsymbol{u})}{\partial \boldsymbol{r}_I^{IB}} & \boldsymbol{0}_{2x3} & \boldsymbol{0}_{2x3} \end{bmatrix} \tag{18}$$

Now the chain rule is applied, using Eq. (16) this results in:

$$\frac{\partial h(\boldsymbol{x},\boldsymbol{u})}{\partial \boldsymbol{r}_I^{IB}} = \frac{\partial h(\boldsymbol{x},\boldsymbol{u})}{\partial \boldsymbol{r}_B^{BP}} \frac{\partial \boldsymbol{r}_B^{BP}}{\partial \boldsymbol{r}_I^{IB}} = \frac{\partial h(\boldsymbol{x},\boldsymbol{u})}{\partial \boldsymbol{r}_B^{BP}} (-\boldsymbol{R}_{BI}) \tag{19}$$

working out the partial derivative gives:

$$\frac{\partial h(\boldsymbol{x},\boldsymbol{u})}{\partial \boldsymbol{r}_B^{BP}} = \begin{bmatrix} \dfrac{f}{Z_B^{BP} h_{\text{px}}} & 0 & -\dfrac{f X_B^{BP}}{(Z_B^{BP})^2 h_{\text{px}}} \\ 0 & \dfrac{f}{Z_B^{BP} h_{\text{px}}} & -\dfrac{f Y_B^{BP}}{(Z_B^{BP})^2 h_{\text{px}}} \end{bmatrix} \tag{20}$$

The sensor noise covariance matrix $\boldsymbol{R}$ depends on the number of measurements that is found after the image processing is performed. In the case that only one measurement is found, the measurement vector consists of two pixel values for $\hat{\boldsymbol{p}}_{\text{cof}}$. The $\boldsymbol{R}$-matrix is then as follows:

$$\boldsymbol{R} = \begin{bmatrix} \sigma_{\text{cam}}^2 & 0 \\ 0 & \sigma_{\text{cam}}^2 \end{bmatrix} \tag{21}$$

2. Laser range finder update

The LRF update is only performed if a valid LRF measurement is obtained from PANGU. Equation (11) is used to calculate the expected LRF measurement given the current state estimate $\hat{\boldsymbol{x}}_{\text{filter}}$. The main challenge here is to obtain $\boldsymbol{r}_P^{PL}$, the vector from the center of the asteroid to the LRF contact point L, as sketched in Fig. 6. For this calculation, the ellipsoid shape model is used. This is not a perfect match for the true shape model, but it is assumed to be the best available shape model given the prior knowledge. The intersection of the Z-axis of $\mathcal{F}_{\mathcal{B}}$ and the ellipsoid is calculated. This calculation is derived in Appendix A.

The Jacobian is calculated as follows. First, the part in Eq. (11) that depends on the filter state $\boldsymbol{x}$ is identified to be $\boldsymbol{r}_P^{PB}$, related to the filter state through $\boldsymbol{r}_I^{IB}$:

$$\boldsymbol{r}_P^{PB} = \boldsymbol{R}_{PI}(\boldsymbol{r}_I^{IB} - \boldsymbol{r}_I^{IP}) \tag{22}$$

The measurement equation $z = h(\boldsymbol{x},\boldsymbol{u})$ for the LRF is given in Eq. (11). The Jacobian of this equation is then:

$$\boldsymbol{H}_x = \frac{\partial h(\boldsymbol{x},\boldsymbol{u})}{\partial \boldsymbol{x}} = \begin{bmatrix} \dfrac{\partial h(\boldsymbol{x},\boldsymbol{u})}{\partial \boldsymbol{r}_I^{IB}} & \boldsymbol{0}_{1x3} & \boldsymbol{0}_{1x3} \end{bmatrix} \tag{23}$$

Now the chain rule is applied:

$$\frac{\partial h(\boldsymbol{x},\boldsymbol{u})}{\partial \boldsymbol{r}_I^{IB}} = \frac{\partial h(\boldsymbol{x},\boldsymbol{u})}{\partial \boldsymbol{r}_B^{PB}} \frac{\partial \boldsymbol{r}_B^{PB}}{\partial \boldsymbol{r}_I^{IB}} = \frac{\partial h(\boldsymbol{x},\boldsymbol{u})}{\partial \boldsymbol{r}_B^{PB}} \boldsymbol{R}_{PI} \tag{24}$$

The remaining partial derivative to complete the Jacobian is given by:

$$\frac{\partial h(\boldsymbol{x},\boldsymbol{u})}{\partial \boldsymbol{r}_B^{PB}} = \frac{\partial \left\| \boldsymbol{r}_P^{PL} - \boldsymbol{r}_P^{PB} \right\|}{\partial \boldsymbol{r}_B^{PB}} = \frac{\boldsymbol{r}_P^{PL} - \boldsymbol{r}_P^{PB}}{\left\| \boldsymbol{r}_P^{PL} - \boldsymbol{r}_P^{PB} \right\|} \tag{25}$$

The sensor noise covariance matrix $\boldsymbol{R}$ represents the uncertainty in the LRF measurement, which is one-dimensional: $R = \sigma_{\text{LRF}}^2$.

E. Reference landing scenario

Now that the EKF is complete, a reference landing scenario is defined. The nominal flight time is 4 hours and the starting position is about 6770 m above the surface of the secondary asteroid. The starting position is in the plane of rotation of the secondary around the primary. The target position that is reached after 4 hours is 300 m above the outward facing pole of the secondary. This infers that somewhere along the trajectory, the primary will appear behind the secondary (Fig. 4), triggering a shutdown of the simulation. The reference trajectory is chosen such that this overlapping of the two bodies in the image only occurs at the very final moments of the simulation when the spacecraft is around 550 m above the surface. By default, the camera and LRF are always pointed at the secondary asteroid. The reference trajectory of the spacecraft is shown in Fig. 7, together with the movement of the asteroids and the Sun direction. The shadow projection onto the YZ-plane shows that the motion of the asteroids and spacecraft is in the plane of rotation of the binary system.

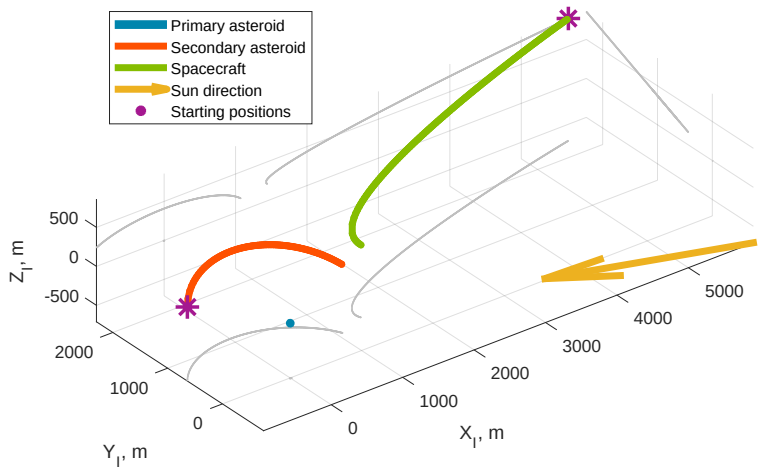

Fig. 7 Trajectory of the primary, secondary, and the spacecraft in the reference landing scenario. Note that the illumination conditions are favorable due to the low Sun phase angles.

F. Initial filter setup and tuning

The initial filter setup and tuning consists of three parts. First, the tuning of the $\boldsymbol{Q}$- and $\boldsymbol{R}$-matrices, the initial $\boldsymbol{P}$-matrix, and the initial filter state are described. Then, the consistency of the filter is verified and typical performance characteristics of the filter are identified. Finally, the effects of various pointing directions for the camera and LRF are examined, followed by a summary of the default EKF configuration after tuning.

1. Filter tuning

The filter tuning process is an iterative process in which the tuning parameters are changed to satisfy the requirements. In this process, the sensitivities of the filter become clear, leading to additional information that is used in the tuning process. The requirement for the position knowledge is that the 3σ uncertainty in the position is less than 10% of the altitude.

The filter state is initialized with the true values of the states, meaning that there is initially no state estimation error. The state estimation error is defined as:

$$\boldsymbol{\Delta} = \boldsymbol{x}_{\text{true}} - \hat{\boldsymbol{x}}_{\text{filter}} \tag{26}$$

For the process noise covariance matrix $\boldsymbol{Q}$, the previously mentioned values of $\sigma_{\text{acc}} = 2.8284 \times 10^{-4}$ m/s^2 and $\sigma_{\text{acc,bias}} = 2.8284 \times 10^{-5}$ m/s^3 are used as a first guess. The results with these values are satisfactory and no further tuning is performed. For the sensor noise covariance matrix $\boldsymbol{R}$, trial and error shows that values of 10 px for σ_{cam} and 15 m for σ_{LRF} give good performance. The state estimation error stays well within the 3σ bounds for the majority of the simulation time and the initial convergence time is around 200 s. For the initialization of the state estimation error covariance matrix $\boldsymbol{P}$, trial and error is used to find a matrix that allows the EKF to quickly converge, without allowing the state estimation error to escape the predicted 3σ bounds. This results in the following matrix:

$$\boldsymbol{P}_0 = \begin{bmatrix} \boldsymbol{\sigma}^2_{\text{pos},0} & \boldsymbol{0}_{3x3} & \boldsymbol{0}_{3x3} \\ \boldsymbol{0}_{3x3} & \boldsymbol{\sigma}^2_{\text{vel},0} & \boldsymbol{0}_{3x3} \\ \boldsymbol{0}_{3x3} & \boldsymbol{0}_{3x3} & \boldsymbol{\sigma}^2_{\text{acc,bias},0} \end{bmatrix} \tag{27}$$

with $\sigma_{\text{pos},0} = 8$ m, $\sigma_{\text{vel},0} = 0.1$ m/s, and $\sigma_{\text{acc,bias},0} = 0.005$ m/s^2. The requirement on the 3σ uncertainty in the position is met for the reference trajectory.

2. Filter consistency and performance characteristics

A consistent state estimator must satisfy two requirements: the estimation errors (i) are zero-mean, and (ii) have a covariance matrix smaller or equal to the one calculated by the filter [35]. To test the developed EKF for consistency,

ideal measurements are generated for the LRF using Eq. (11) and for the camera using Eq. (17). This is done by feeding knowledge of the true system state from the simulator into these equations. To these ideal measurements, zero-mean white noise with known variance is added. The EKF is then given these variances through the $\boldsymbol{R}$-matrix. The filter output must then satisfy the two requirements associated with a consistent state estimator.

More realistic measurements are introduced in two steps. First, the ideal camera measurement is replaced by the PANGU images and subsequent image processing. The effect of this change on the position estimation error is shown in Fig. 8. Several observations can be made from this figure:

1) The EKF is consistent when ideal measurements with known noise characteristics are used. Calculations show that the error signal mean is close to zero: 2 m, 0.02 m/s, and $3{\times}10^{-5}$ m/s^2, for the position, velocity, and accelerometer bias signal components. The estimation error statistics are in agreement with the EKF's calculated covariances. Only two simulations with idealized measurements are done in this work. While both simulations suggest that the filter is consistent, more simulations are required to make a definitive statement about the consistency of the EKF.
2) The flight trajectory is such that for the majority of the flight, especially the first 8000 seconds, the LRF and camera are pointed along the negative X-axis of $\mathcal{F}_I$. The LRF is responsible for most of the state estimation in this direction. Therefore, introducing the camera measurements from PANGU has little effect on the position estimation error in the X-direction.
3) The position estimation errors are smaller in the X-direction compared to the Y- and Z-direction. This is because the LRF is more accurate than the (indirect) distance measurements from the camera images.
4) Note the jump in the 3σ bounds around 2800 seconds, best visible in the position estimation error for the Y-direction. This is due to the loss of visibility of the primary asteroid. As the measurement is lost, the uncertainty in the state estimate increases again.
5) The 3σ bounds along the Y- and Z-direction, which are determined mainly by the camera measurements, keep converging as the spacecraft comes closer to the asteroid. This behavior can be explained as follows: imagine observing an asteroid at 6 km distance, with the camera pointed at the exact center of brightness of the asteroid. If the asteroid now moves 10 px in the image frame, the asteroid would have to move a large distance to make this shift. Repeat the same experiment now with an asteroid at 600 m distance. The distance that the asteroid needs to move to achieve this 10 px shift is now much smaller. In other words, the estimation error in meters, associated with a 10 px uncertainty, gets lower and lower as the distance to the observed object decreases.
6) The estimation error starts to escape the 3σ bounds in the final part of the simulation. This is caused by errors in the image processing that are becoming increasingly large as the irregularly shaped object gets closer. Take for example Fig. 4. The center of brightness of the secondary asteroid will be very far off the true center of figure, causing these errors.

The next development step is to introduce the LRF measurement from PANGU. The result of this step is shown in Fig. 9. We see that the estimation error in the X-direction has increased with the implementation of the PANGU LRF measurement. This is caused by the mismatch between the LRF measurement and the ellipsoid model used in $z = h(\boldsymbol{x}, \boldsymbol{u})$.

3. Pointing direction tuning

To understand which camera/LRF pointing strategy yields the best results, three tests are executed. The camera/LRF pointing is chosen to be either primary, secondary, or at the midpoint in between the two asteroids. Because the goal is to land the spacecraft on the secondary, the spacecraft will always re-point to the secondary in the final phase of flight. The switching point is determined by the image processing: once one of the two asteroids is lost out of sight, the spacecraft reorients itself to point to the secondary asteroid. This maneuver is implemented as an instant change of attitude.

Pointing either primary and then secondary, or always pointing secondary, yields similar results. Pointing secondary is the preferred option as fewer maneuvers are required. The results of pointing at the midpoint, compared to pointing secondary, are shown in Figs. 10 and 11. Several observations are made:

1) The state estimation errors in the X-direction are much larger when pointing at the midpoint. This is due to the loss of the LRF when pointing at the midpoint between the asteroids. From the two camera measurements, the distance to the asteroids can still be determined, although less accurate than with the LRF.
2) The timestep that an asteroid is lost out of sight and the spacecraft reorients to point secondary is delayed, from around 2800 seconds when pointing secondary to 8600 seconds when pointing at the midpoint.
3) After the reorientation maneuver, the two curves overlap. This is expected, as the measurements and trajectory

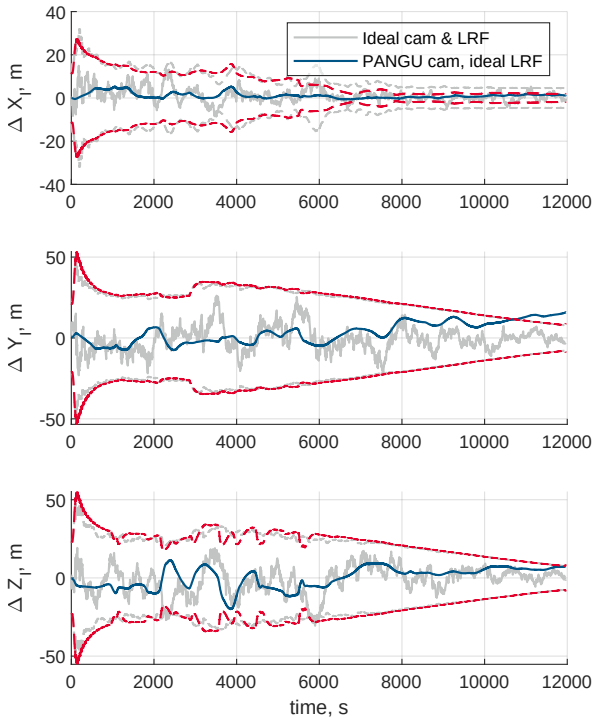

Fig. 8 *I*-frame position estimation errors, including error 3σ bounds. Ideal camera measurements compared to PANGU.

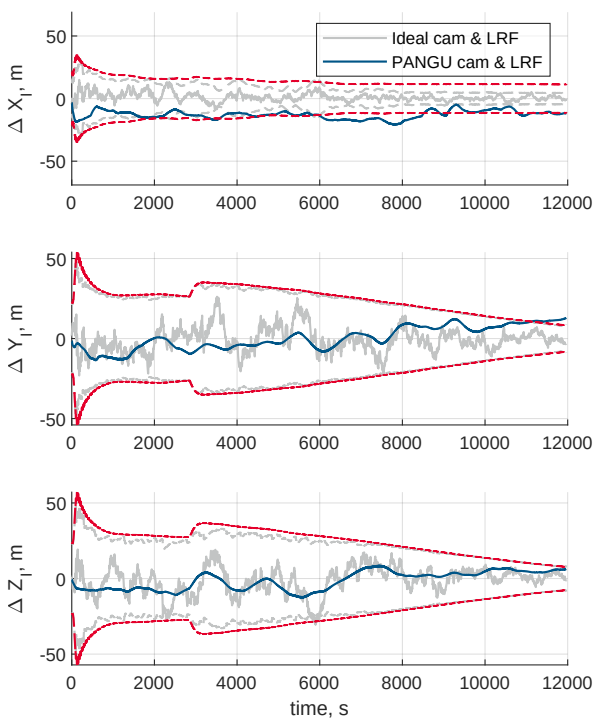

Fig. 9 *I*-frame position estimation errors, including error 3σ bounds. Ideal measurements compared to PANGU camera and LRF measurements.

are the same for both simulations.

The key outcome of this test is that while navigation without the LRF is not preferred due to the larger state estimation errors, it can be used as a back-up if the LRF fails, or in an orientation phase where the spacecraft changes its pointing such that the LRF is not always available.

4. Navigation filter default configuration

The default configuration for the navigation filter that is established after this initial testing phase is given in Table 3.

G. Verification and validation

Verification and validation is done to make sure that the models are implemented correctly, and to check that the produced results match reality. Several steps are taken to verify the results in this work. Validation is left as a recommendation for future work. Examples of verification efforts are: the polyhedron gravity field is verified to approach a point mass model at far distances, the SPICE kernel is verified to output orbits in accordance with [22], the EKF consistency is checked, the LRF ellipsoid model is compared to the PANGU LRF output for a full rotation around the asteroid to verify the correct orientation and dimensions of the ellipsoid model, and the image processing is validated with numerous edge-cases. The PANGU LRF verification is shown in more detail in Appendix B.

V. Results

This section extends on the results from the previous section by testing the behavior of the EKF in three different ways. First, the sensitivity to the initial position of the spacecraft is studied, followed by an analysis on how the EKF responds to errors in the initialization of the filter state, a very relevant test because the deployment from the mothership is imperfect and demands some robustness of the navigation solution. Finally, the sensitivity of the EKF to three common image imperfections is investigated.

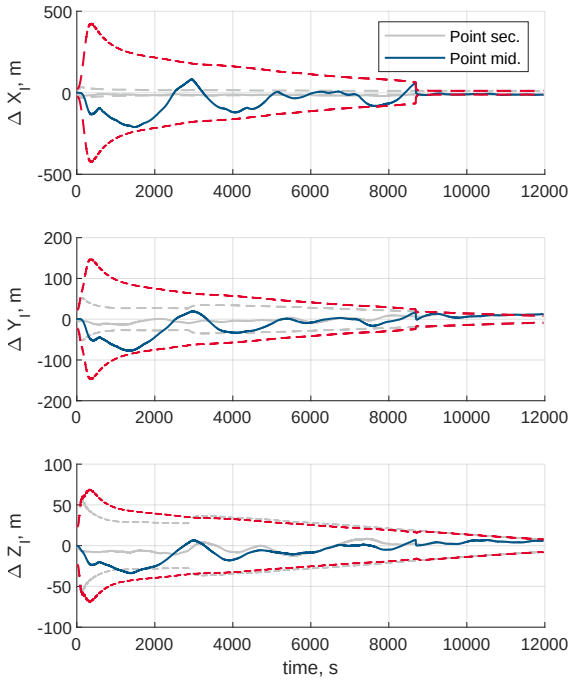

Fig. 10 ***I*-frame position estimation errors, including error 3σ bounds. Pointing secondary compared to pointing at the midpoint.**

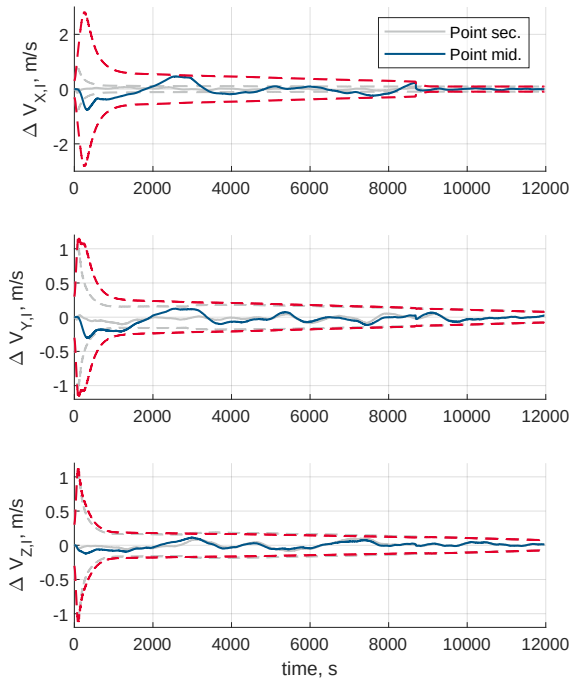

Fig. 11 ***I*-frame velocity estimation errors, including error 3σ bounds. Pointing secondary compared to pointing at the midpoint.**

Table 3 Navigation filter settings in the default configuration.

Setting	Value	Unit
Pointing strategy	Secondary	-
Approach trajectory	In-plane	-
Starting altitude	6770	m
Final altitude	300	m
Flight time	4	h
Accelerometer sample time	0.125	s
Camera & LRF sample time	5	s
σ_{acc}	2.8284×10^{-4}	m/s^2
$\sigma_{\text{acc,bias}}$	2.8284×10^{-5}	m/s^3
σ_{cam}	10	px
σ_{LRF}	15	m
Initial estimation error	0	-

A. Initial position sensitivity

The initial position can be chosen based on several factors: minimum fuel consumption, favorable lighting conditions, minimal overlap of the two asteroids in the image, to name a few. It could also be that the deployment of other spacecraft attached to the mothership have a higher priority and therefore a sub-optimal starting position is inevitable. Therefore, the sensitivity to the starting position is studied. A semi-sphere of 90 starting points is calculated, with the middle point located on the shell at the default starting position. The semi-sphere is positioned such that the Sun is usually behind the spacecraft, although the Sun phase angles can get very large for some starting positions. The other half of the sphere is not considered because either the lighting conditions will be very challenging, or the spacecraft must fly around the

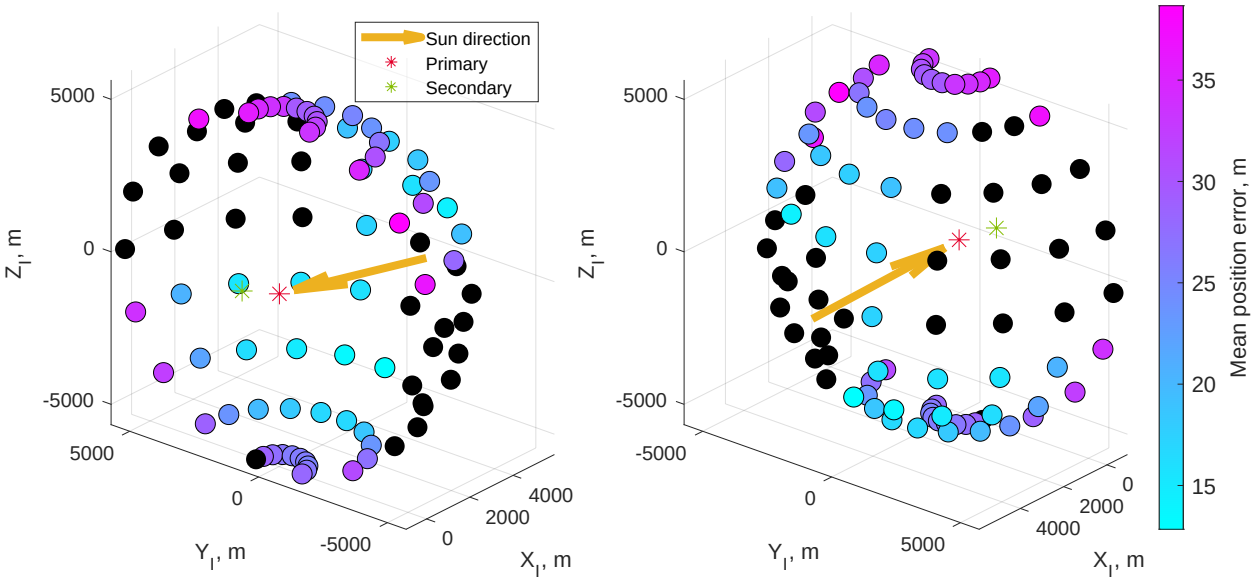

Fig. 12 Mean position error for different starting positions. Black dots indicate trajectories with final altitude above 600 m.

primary asteroid to get to its target final position. The parameters as described in Table 3 are used. The metric used to summarize the performance of the EKF in a particular run is the mean position error. This error is calculated as follows:

$$\text{Mean position error} = \frac{\sum_{i=1}^{n} \sqrt{\Delta_{x,i}^2 + \Delta_{y,i}^2 + \Delta_{z,i}^2}}{n} \tag{28}$$

where n is the total number of filter state samples in a run.

Figure 12 shows the results from two different viewing angles. The black dots indicate starting conditions that resulted in a trajectory that ended before an altitude of 600 m was reached. This is the result of the simulation being stopped by the image processing due to asteroids overlapping in the image, step 8 of Algorithm 1.

Several observations are made based on Fig. 12:

1) The black dots indicate that overlapping asteroids in the image are a major weakness of the current image processing implementation, limiting the scope of trajectories that can be flown.
2) Approaching the binary system out-of-plane, either from the top or the bottom, partially mitigates the previous shortcoming because the bodies will not overlap except for in the final moments of the high-altitude phase.
3) There is a relationship between the Sun phase angle and the mean position error.

The mismatch between the LRF measurement and the ellipsoid model, as well as the impact of irregular shapes and higher Sun phase angles on the center of figure estimation, have a major impact on the state estimation. To investigate which one of these is dominating the error behaviour observed in Fig. 12, the mean position error is shown against the mean Sun phase angle for the secondary asteroid, Fig. 13. The relationship between the independent variable x (mean Sun phase angle of the secondary) and the the dependent variable y (mean position error) is fit using linear regression. The assumed relationship is based on Eq. (9), because the image processing error is proportional to the Sun phase angle as well. The image processing error trickles down into the state estimation error, thus it is reasonable to expect the mean position error to follow a similar trend. The equation that is fit is:

$$y = \theta_0 + \theta_1 \arctan\left(\frac{8\pi R}{3\bar{r}} \sin^2\left(\frac{x}{2}\right)\right) \tag{29}$$

with $\bar{r}$ the mean altitude above the secondary asteroid, which is 3462 m for all runs that reach below 600 m of altitude. Linear regression yields $\theta_0 = 12.2$ and $\theta_1 = 273.0$. The adjusted R^2 is 0.829, indicating that the mean Sun phase angle of the secondary plays a major role in a run's mean position error.

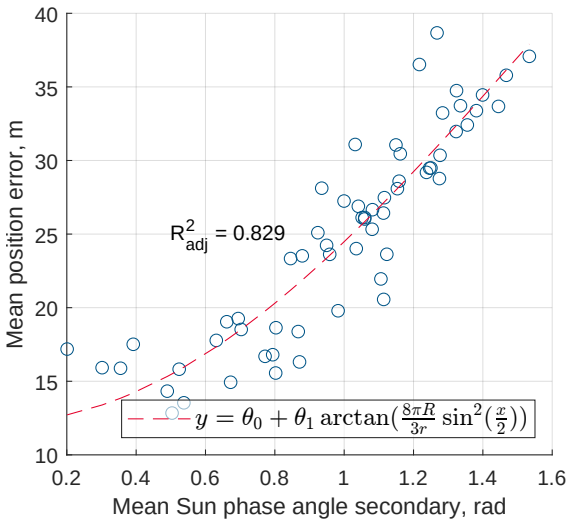

Fig. 13 Relationship between the mean Sun phase angle of the secondary asteroid and the mean position error for each colored starting point in Fig. 12.

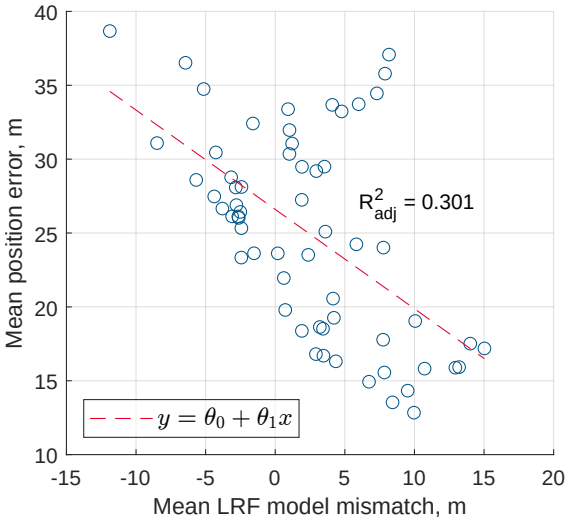

Fig. 14 Relationship between the mean LRF model mismatch and the mean position error for each colored starting point in Fig. 12.

Table 4 Summary of state estimation results for all colored starting points in Fig. 12. Worst value for each metric is highlighted for position, velocity, and accelerometer bias states.

	Position			**Velocity**			**Acc. bias**		
	X_I, m	Y_I, m	Z_I, m	X_I, m/s	Y_I, m/s	Z_I, m/s	X_B, m/s^2	Y_B, m/s^2	Z_B, m/s^2
Max RMS error	35.1	24.4	13.0	0.08	0.05	0.05	4.63×10^{-4}	4.04×10^{-4}	2.99×10^{-4}
Max RMS 3σ	28.9	26.8	25.5	0.21	0.20	0.19	1.655×10^{-3}	1.657×10^{-3}	1.436×10^{-3}
Max-max error	74.9	21.8	34.8	0.69	0.11	0.16	4.415×10^{-3}	3.795×10^{-3}	2.867×10^{-3}
Max final error	27.9	21.5	15.5	0.06	0.05	0.04	1.57×10^{-4}	1.38×10^{-4}	2.64×10^{-4}
Max final 3σ	11.3	9.8	8.5	0.09	0.08	0.08	4.78×10^{-4}	4.78×10^{-4}	5.20×10^{-4}

The same procedure is repeated for the LRF model mismatch. An attempt is made to describe the relationship as linear, resulting in an adjusted R^2 of 0.301. The data points and fitted line are shown in Fig. 14. The mean LRF model mismatch is 2.36 m, with a standard deviation of 8.28 m. The effect of the LRF model mismatch on the mean position error is not clear from this analysis, most likely because the image processing errors due to high Sun phase angles are dominating the error behavior. Note that only one ellipsoid model is tested with only one shape model in PANGU. For other (worse) shape models, the effect of the LRF model mismatch might be stronger.

Figures 15 and 16 show the position and velocity errors in the I-frame for all 61 runs that reach an altitude below 600 m. The run with the highest mean position error is highlighted. The centroid-based image processing struggles to estimate $\hat{\boldsymbol{p}}_{\text{cof}}$ as the spacecraft moves closer to the asteroid. This is because the effect of the irregular shape and potentially high Sun phase angles is much more dominant at close range. Due to these two effects, the assumption that $\hat{\boldsymbol{p}}_{\text{cof}}$ is a good approximation for $\boldsymbol{p}_{\text{cof}}$ no longer holds. The results of the starting position sensitivity analysis are summarized in Table 4.

B. Filter initialization error sensitivity

The EKF is initialized with a guess for the filter state. This guess is provided by the navigation system of the mothership, and is subject to additional uncertainty because the detachment of the spacecraft from the mothership is prone to errors and comes with uncertainties. The deployer ejection velocity can be adjusted up to a maximum value of 5 cm/s [36]. This does however not mean that the uncertainty is also 5 cm/s, because there are also uncertainties in the velocity of the mothership itself. In [37] the landing scenario for the Milani cubesat to land on Dimorphos is studied,

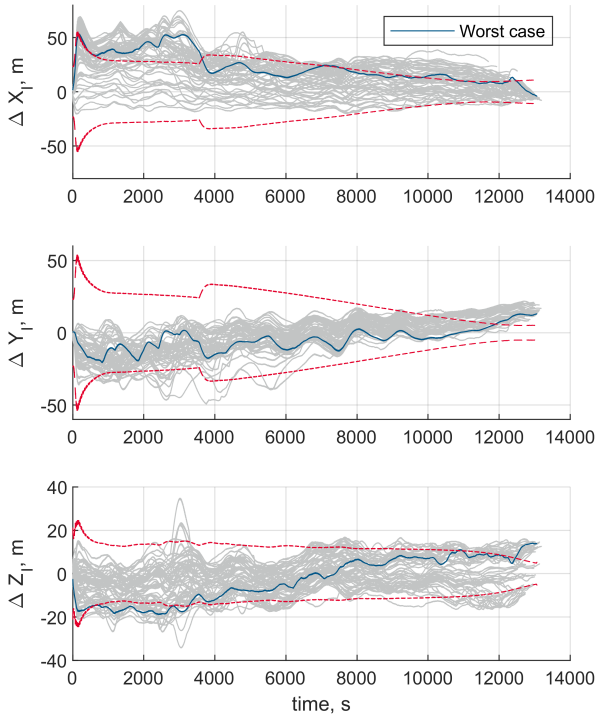

Fig. 15 I-frame position estimation errors for all colored starting points in Fig. 12. Error 3σ bounds are shown for the worst case.

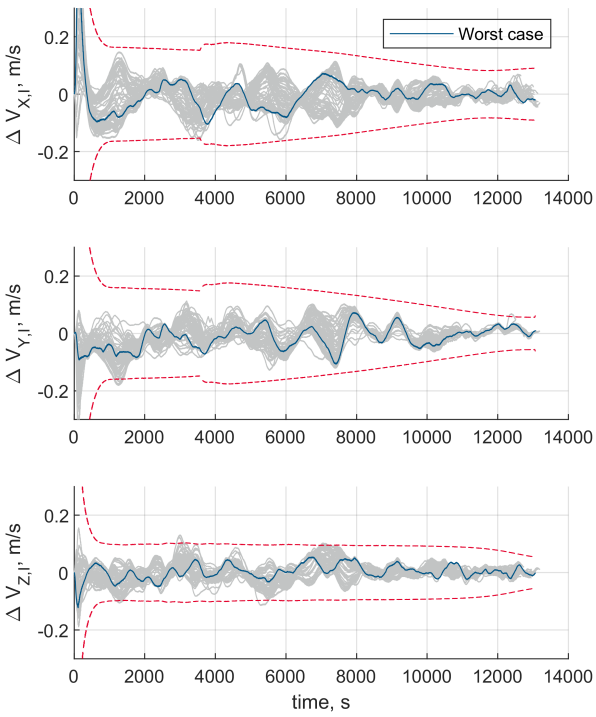

Fig. 16 I-frame velocity estimation errors for all colored starting points in Fig. 12. Error 3σ bounds are shown for the worst case.

and values of 13.3 m and 0.33 m/s (1σ) are used for the initial state uncertainty. In this work, very conservative values are used for the initial uncertainty, to push the EKF to its performance bounds in the reference landing scenario. The initial state error is calculated as follows:

$$\boldsymbol{x}_0 = \begin{bmatrix} \boldsymbol{r}^{IB}_{I,\text{true}} + \boldsymbol{\eta}_{\text{pos}} \\ \dot{\boldsymbol{r}}^{IB}_{I,\text{true}} + \boldsymbol{\eta}_{\text{vel}} \\ \boldsymbol{b}_{\text{acc},B,\text{true}} + \boldsymbol{\eta}_{\text{acc.bias}} \end{bmatrix} \tag{30}$$

where $\boldsymbol{\eta}$ is a 3x1 vector whose components are randomly drawn from a normal distribution:

$$\eta_{\text{pos},x} \sim \mathcal{N}\left(0, \sigma^2_{\text{pos}}\right) \tag{31}$$

The following noise intensities are used: $\sigma_{\text{pos}} = 30$ m, $\sigma_{\text{vel}} = 5$ m/s, and $\sigma_{\text{acc.bias}} = 0.01$ m/s^2. These values are also used for the initialization of the $\boldsymbol{P}$-matrix. In total 400 simulations are done with this random initialization, the results of which are shown in Figs. 17 and 18. The worst case that still converges is highlighted in the figures and is selected for further investigation. This specific run started with the 5th worst initialization error in terms of position, and the 6th worst accelerometer bias initialization. It thus represents a very extreme case within the dataset and the EKF has trouble converging for this extreme initialization error. By successfully converging in 390 of the 400 simulations with these very conservative initial uncertainties, the EKF proves to be robust to large uncertainties in the initial filter state. This is most likely due to the good initial observability with two asteroids in the camera frame on top of the LRF measurement.

C. Image imperfections sensitivity

The images that are rendered in PANGU have thus far not included any common imperfections. Imperfections such as radial distortion (Fig. 19a), an out-of-focus image (Fig. 19b), and salt & pepper noise (Fig. 19c) are investigated to evaluate the robustness of the EKF and image processing to these effects. Radial distortion is a common image imperfection associated with the lens of the camera, and Hendrycks (2019) mentions several other common image

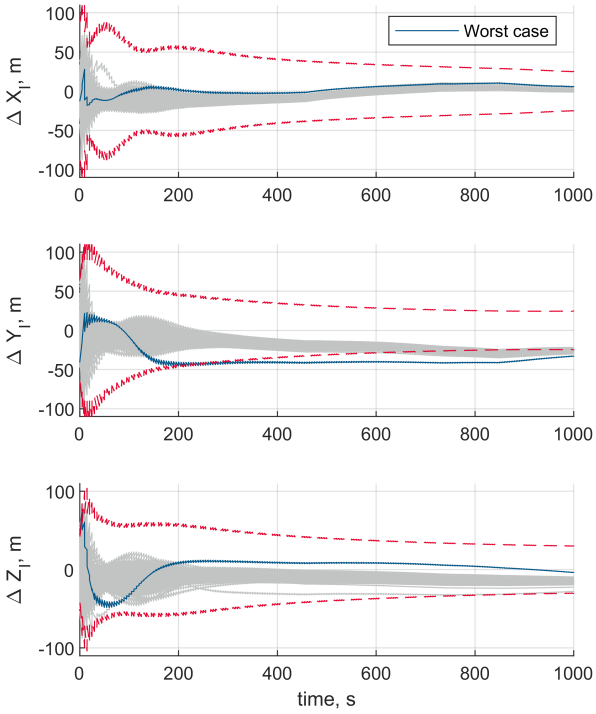

Fig. 17 I-frame position estimation errors for 400 random filter state initializations calculated with Eqs. (30) and (31). Error 3σ bounds are shown for the worst case.

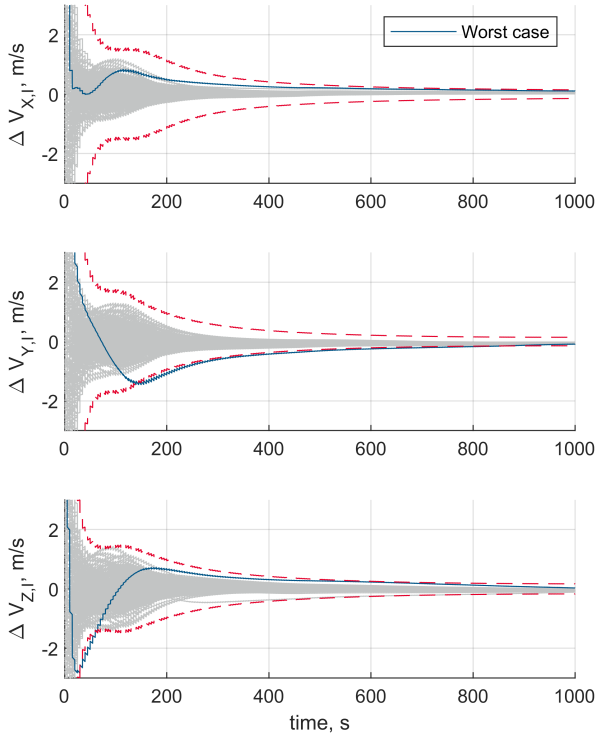

Fig. 18 I-frame velocity estimation errors for 400 random filter state initializations calculated with Eqs. (30) and (31). Error 3σ bounds are shown for the worst case.

imperfections [38]. Two overarching categories of imperfections found in [38] are identified and tested in this paper. These are noise imperfections (Gaussian noise, shot noise, impulse noise) and blur imperfections (defocus blur, frosted glass blur, motion blur, zoom blur). The image processing is expected to respond similarly to the imperfections within these two categories and therefore only one type of imperfection is tested from each category. Blur imperfections are simulated using a Gaussian blur filter, and noise imperfections are simulated using the salt & pepper noise filter. MATLAB functions from the Image Processing and Computer Vision toolbox[‖] are used to implement the imperfections. The imperfections are applied to the image as soon as it is produced by PANGU, after which the image is sent to the image processing.

To create the radial distortion effect, PANGU's initialization function is changed. This results in the mapping of every undistorted point (i, j) to the observed distorted point (i', j') using Eqs. (32-34). The values for the coefficients K in Eq. (34) that are used are given in Table 5. The constants that are not mentioned are 0.

$$\begin{bmatrix} i' - i_0 \\ j' - j_0 \end{bmatrix} = C(R) \begin{bmatrix} i - i_0 \\ j - j_0 \end{bmatrix} \tag{32}$$

$$R = \sqrt{(i - i_0)^2 + (j - j_0)^2} \tag{33}$$

$$C(R) = 1 + K_0 + K_1 R + K_2 R^2 + K_3 R^3 + K_4 R^4 + \cdots \tag{34}$$

The values for the standard deviation of the smoothing kernel and the noise density are also given in Table 5. The standard deviation of the smoothing kernel determines the Gaussian function that is used to construct a convolution matrix that is applied to the original image [39]. The salt & pepper noise density determines the percentage of pixels that are affected by the noise. Each effect is studied separately, thus a total of 8 simulations are done. These are then

[‖] `https://de.mathworks.com/products/image.html`, last accessed 2023/04/08

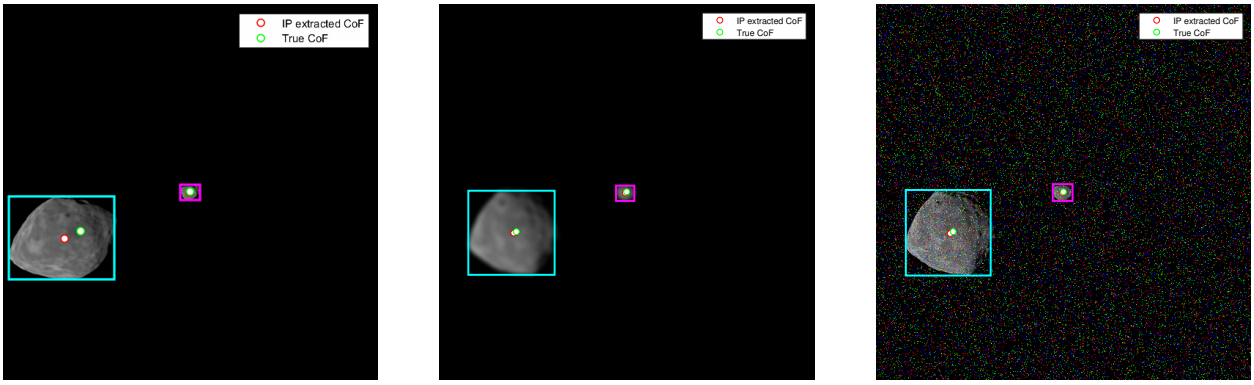

(a) Radial distortion, K_2 = 2e-06, K_4 = 2e-11. **(b) Gaussian blur, σ_{blur} = 3.** **(c) Salt & pepper noise, noise density = 8%.**

Fig. 19 The three types of image imperfections that are studied

compared to a reference simulation without any imperfections. The simulation settings are as described in Table 3, with one change: the starting altitude is chosen to be 8589 m. The reason for this change is that the radial distortion can cause the primary asteroid to touch the border of the image at the start. This would mean that the centroid measurement from the primary asteroid is ignored in the EKF. With a more distant initial position, the primary is always completely visible in the image at the start. The effect of the radial distortion is most dominant at the edges of the image, and the effect on the secondary will be limited because it is in the center of the image. Therefore, changing the altitude to include measurements of the primary asteroid is important to analyse the effects of radial distortion. This effect is also observed in Fig. 19a, where for the primary the estimated center of figure is far off the true center of figure.

Table 5 Values used for the generation of image imperfections. Note that only one effect is applied at a time.

	Values			
Radial distortion coefficients (K_2, K_4)	(0,0)	(1e-6, 1e-11)	(2e-6, 2e-11)	-
Gaussian blur smoothing kernel σ	0	1	3	5
Salt & pepper noise density	0%	2%	5%	8%

For the reference settings described in Table 3, with a starting altitude of 8589 m, there is almost no impact on the EKF performance when the images are subject to Gaussian blur or salt & pepper noise. At all three intensity levels, the mean position error does not change more than 3% compared to the reference. This worst case number is observed for the Gaussian blur with a smoothing kernel σ of 5, resulting in a change of the mean position error from 18.54 m (without blur) to 19.10 m (with blur).

The impact of radial distortion on the state estimation is significant, as can be seen in Figs. 20 and 21. The position and velocity errors are shown for three different levels of distortion, level 0 up to level 2, corresponding to the values in Table 5. It is clear that larger distortion coefficients lead to an increase in the state estimation errors. The mean position error during the first 5000 seconds of the three simulations grows with each increase in radial distortion: from 21.66 m, to 41.28 m, to 59.37 m for the highest level.

Because the primary asteroid touches the border of the camera image earlier with a highly distorted image, the instantaneous reorientation to point at the secondary asteroid occurs at varying timesteps for all three levels of distortion. Once the primary asteroid is out of view, the estimation results are the same. This is reflected in the mean position error in the period after the first 5000 seconds: the mean position errors are then within 20 cm of each other for all three distortion levels. This is expected, because the effect of radial distortion is a function of the distance R from the center of the image, Eqs. (32-34). The distortion effect is therefore smaller in the center of the image, which is exactly where the secondary asteroid is located. On top of this, the asteroid is distorted equally in all directions away from the center of the image. The effect of the distortion on the center of figure estimation is not entirely symmetrical because of the irregular 3D shape model and non-zero Sun phase angle, but the mean position errors show that the state estimation errors due to the distortion effect are decreased significantly when only an asteroid in the center of the image is observed.

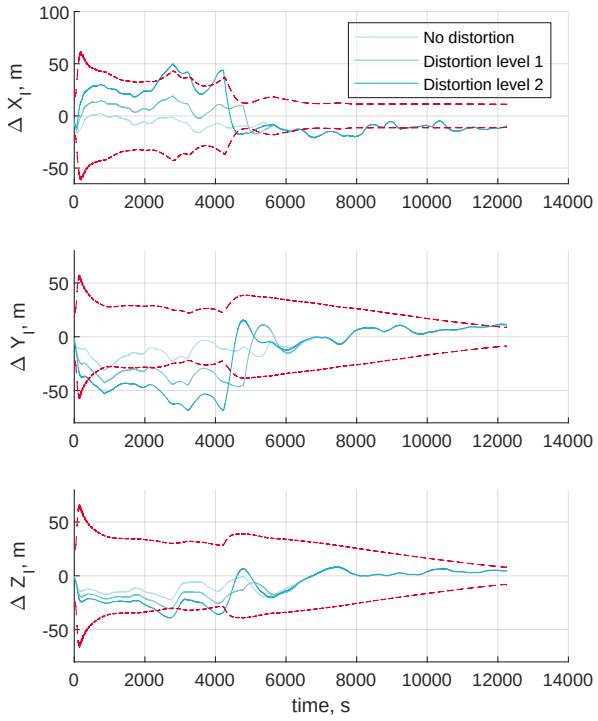

Fig. 20 I-frame position estimation errors for three levels of radial distortion given in Table 5. 3σ bounds shown for the highest level of radial distortion.

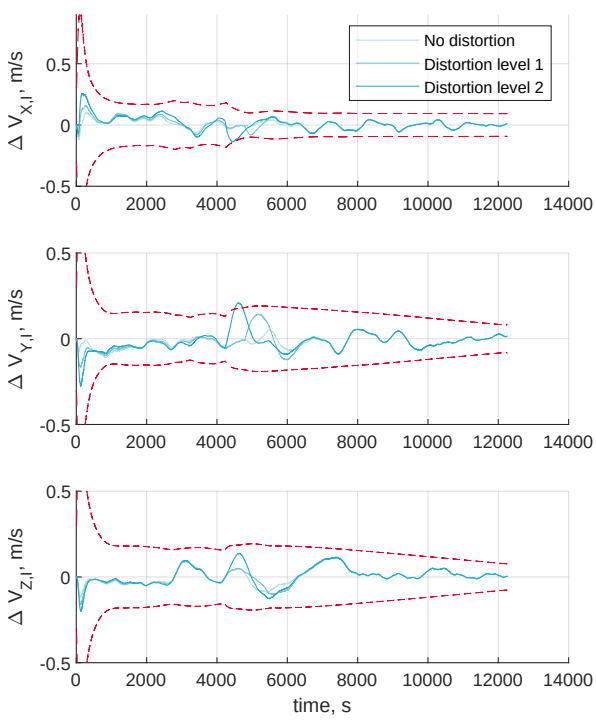

Fig. 21 I-frame velocity estimation errors for three levels of radial distortion given in Table 5. 3σ bounds shown for the highest level of radial distortion.

VI. Conclusions and recommendations

This work proposes an autonomous navigation solution for small spacecraft in a binary asteroid environment. It extends on previous work that investigated the effectiveness of laser range finders and cameras for navigation in (binary) asteroid environments. This section concludes the work done in this paper and gives a list of recommendations for future work.

A. Conclusions

An extended Kalman filter with nine parameters in the state vector is shown to successfully estimate the spacecraft state in an inertial reference frame. Prior knowledge of the asteroid ephemeris and ellipsoidal shape model is required to connect the relative measurements to the inertial frame. The image processing that extracts measurements from the camera images is identified as a pivotal component with a large influence on the performance of the filter. Its performance is impacted by high Sun phase angles and irregular asteroid shapes. It is shown that for an irregular asteroid shape and for high Sun phase angles, the quality of the measurements is still sufficient to perform the state estimation. Furthermore, the navigation solution is shown to be robust to large uncertainty in its initial state estimate. The navigation solution converges for 390 out of 400 simulation runs with conservative initialization errors. The filter state is also observable without the laser range finder, as long as there is good visibility of both asteroids. Finally, the navigation solution was tested with distorted and noisy camera images, to which the filter responded in a robust manner without any failure. The navigation solution developed in this work is therefore a robust option for medium to close range navigation in a binary asteroid environment.

B. Recommendations

This research leaves several important questions open that need to be answered in future work. Recommendations following the research presented in this paper are listed below.

Include attitude control and estimation: The pointing algorithm currently relies on the perfect knowledge of the state and asteroid ephemeris. This is an essential part to obtain the camera measurements that are inputs for the EKF.

In reality, this perfect knowledge is not available and therefore the spacecraft must determine and control its attitude. The desired pointing direction of the camera and LRF must be based on image data. Inclusion of such an image-based pointing algorithm leads to a more complete understanding of the capabilities of a spacecraft using this navigation system.

Improve the image processing: The issue of overlapping asteroids needs to be solved to increase the deployability of the navigation system. The current image processing requires permanent separation of the two asteroids in the frame. This limitation needs to be removed such that a wider range of approach trajectories can be flown.

Improve the center of figure detection: This will increase robustness to high Sun phase angles and to irregular asteroid shapes. Possible improvements are to exploit prior knowledge about the asteroid shape with a data-driven approach as proposed in [40], or by using AI-based image processing such as proposed in [41].

Test more image imperfections: This work includes Gaussian blur, radial distortion, and salt & pepper noise. Additional testing could for example include motion blur, over & under exposure, readout/reset smear, and color jitter.

Add more sensors: Adding more sensors potentially increases the robustness and performance of the filter. More LRF's, or a flash lidar could be added, as demonstrated in [5]. Adding a second camera allows the navigation system to obtain LOS measurements of both asteroids without being limited by the FOV of a single camera. These measurements can then be used with a triangulation technique, as presented in [13].

Validation: Testing the system in the real world is necessary to validate the results obtained in this paper. Pseudo-validation in the form of a comparison between the results in this paper and independently published work in literature is a valuable in-between step before real-world validation. A good candidate for real-world validation of the image processing is ESA's GNC Rendezvous, Approach and Landing Simulator (GRALS)**. Fly-bys with other bodies that are encountered on the way to the target asteroid can also be used to validate the navigation system.

Appendix A - Ellipsoid line intersection

The intersection of an ellipsoid and a line is used in $z = h(\boldsymbol{x}, \boldsymbol{u})$ for the laser range finder measurement model. This appendix shows how this intersection is found. First, a line $\boldsymbol{p}$ is defined according to Eq. (35). This line will be in the direction of the z-axis of the B-frame, the boresight direction of the camera and also the direction of the LRF instrument.

$$\boldsymbol{p} = \boldsymbol{v}_0 + t\boldsymbol{v}_1 \tag{35}$$

$$\boldsymbol{v}_0 = (\chi_0, \gamma_0, \zeta_0)^T \tag{36}$$

$$\boldsymbol{v}_1 = (\chi_1, \gamma_1, \zeta_1)^T \tag{37}$$

Here $\boldsymbol{v}_0$ in Eq. (36) is the position of the spacecraft in the ellipsoid-fixed reference frame and $\boldsymbol{v}_1$ in Eq. (37) is the direction that the LRF instrument is pointed in, which is the z-axis of the B-frame. Then, the ellipsoid is defined using Eq. (38). Here a, b, and c are the lengths of the semi-axes of the ellipsoid. For the asteroids, these are provided in [22].

$$\frac{x^2}{a^2} + \frac{y^2}{b^2} + \frac{z^2}{c^2} = 1 \tag{38}$$

Next, the line $\boldsymbol{p}$ is substituted into the ellipsoid equation:

$$\left(\frac{\chi_0 + t\chi_1}{a}\right)^2 + \left(\frac{\gamma_0 + t\gamma_1}{b}\right)^2 + \left(\frac{\zeta_0 + t\zeta_1}{c}\right)^2 = 1 \tag{39}$$

Expanding the terms in Eq. (39) and grouping the terms by their powers of t yields Eq. (40). Finding the solution for t is now only a matter of applying the quadratic formula.

**https://www.esa.int/ESA_Multimedia/Images/2018/05/GRALS_Testbed, last accessed 2023/03/21

$$\left(\frac{\chi_1^2}{a^2}+\frac{\gamma_1^2}{b^2}+\frac{\zeta_1^2}{c^2}\right)t^2+\left(\frac{2\chi_0\chi_1}{a^2}+\frac{2\gamma_0\gamma_1}{b^2}+\frac{2\zeta_0\zeta_1}{c^2}\right)t+\left(\frac{\chi_0^2}{a^2}+\frac{\gamma_0^2}{b^2}+\frac{\zeta_0^2}{c^2}-1\right)=0 \tag{40}$$

Finally, substituting the values found for t back into Eq. (35) yields the intersection points. The intersection point closest to $\boldsymbol{v}_0$ is used as the point of contact of the LRF.

Appendix B - Laser range finder verification

The LRF measurement model uses the ellipsoid-line intersection to calculate the expected LRF measurements. A test is set up in the simulator to check that the implementation is correct. For this test, the spacecraft is placed at a fixed distance of 500 m from the secondary asteroid center of mass. The spacecraft points at the center of mass of the secondary and the LRF measures the distance to the surface. The secondary then completes one full revolution around its center of mass. The experiment setup is visualized in Fig. 22. The LRF measurements are then compared with the expected measurements from the ellipsoid measurement model. By subtracting the LRF measurement from the altitude, the distance from the center of mass to the surface of the asteroid is obtained. With a full revolution of the asteroid, a slice of the asteroid 3D model is obtained. The same can be done for the ellipsoid model. Two tests are done, each test represents a different axis of rotation for the asteroid. The result of one of these tests is shown in the form of a polar plot in Fig. 23. The ellipsoid model captures the overall shape of the asteroid, and its orientation is also correct. This test verifies that the LRF measurement model is implemented correctly.

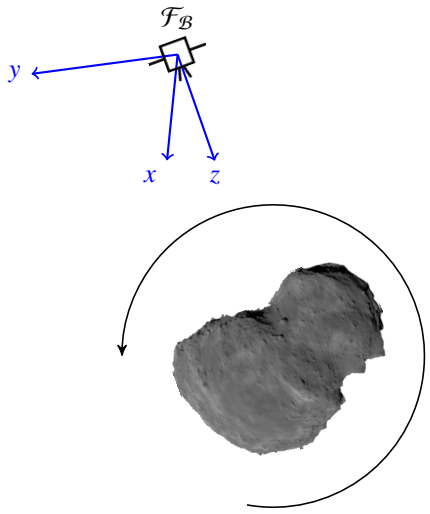

Fig. 22 Sketch of the LRF verification experiment. The secondary asteroid completes one full rotation around one axis.

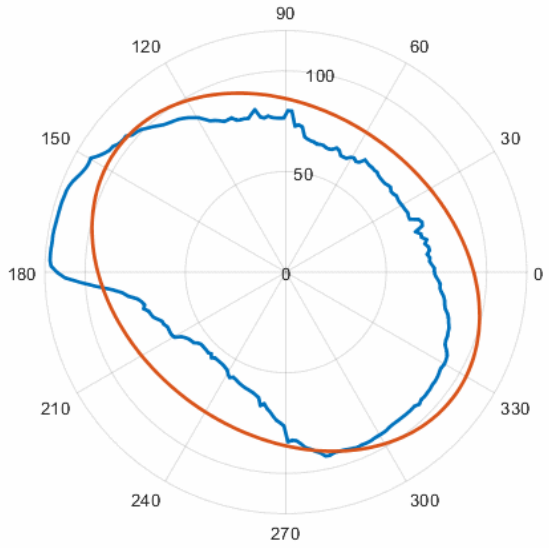

Fig. 23 Polar plot comparing the LRF measurement from PANGU (blue) and the ellipsoid measurements model (orange). Radial distance in m.

Acknowledgments

Peter Elffers thanks Airbus Defence & Space Germany, specifically the TESOA1 GNC/AOCS department, for their support of this project. Special thanks go to Stefan Winkler of Airbus Defence & Space Germany for his guidance and

support of this work. This study is part of the NEO-MAPP project, work package 8, lead by Airbus Defence & Space Germany. This project has received funding from the European Union's Horizon 2020 research and innovation program under grant agreement No. 870377.

References

[1] Cheng, A. F., "Near Earth asteroid rendezvous: mission summary," *Asteroids III*, Vol. 1, 2002, pp. 351–366.

[2] Kawaguchi, J., Fujiwara, A., and Uesugi, T., "Hayabusa—Its technology and science accomplishment summary and Hayabusa-2," *Acta Astronautica*, Vol. 62, No. 10, 2008, pp. 639–647. https://doi.org/10.1016/j.actaastro.2008.01.028.

[3] Ulamec, S., Fantinati, C., Maibaum, M., Geurts, K., Biele, J., Jansen, S., Küchemann, O., Cozzoni, B., Finke, F., Lommatsch, V., Moussi-Soffys, A., Delmas, C., and O´Rourke, L., "Rosetta Lander – Landing and operations on comet 67P/Churyumov–Gerasimenko," *Acta Astronautica*, Vol. 125, 2016, pp. 80–91. https://doi.org/10.1016/j.actaastro.2015.11.029.

[4] De Santayana, R. P., and Lauer, M., "Optical measurements for Rosetta navigation near the comet," *Proceedings of the 25th International Symposium on Space Flight Dynamics (ISSFD), Munich*, 2015.

[5] Dietrich, A., and McMahon, J. W., "Asteroid Proximity Navigation using Flash LIDAR," *AIAA/AAS Astrodynamics Specialist Conference*, American Institute of Aeronautics and Astronautics, 2014. https://doi.org/10.2514/6.2014-4355.

[6] Morley, T., and Budnik, F., "Rosetta Navigation for the Fly-by of Asteroid 2867 Šteins," *Proceedings 21st International Symposium on Space Flight Dynamics-21st ISSFD, Toulouse, France*, 2009.

[7] Synnott, S., Donegan, A., Riedel, J., and Stuve, J., "Interplanetary optical navigation-Voyager Uranus encounter," *Astrodynamics Conference*, American Institute of Aeronautics and Astronautics, 1986. https://doi.org/10.2514/6.1986-2113.

[8] Vetrisano, M., and Vasile, M., "Autonomous navigation of a spacecraft formation in the proximity of an asteroid," *Advances in Space Research*, Vol. 57, No. 8, 2016, pp. 1783–1804. https://doi.org/10.1016/j.asr.2015.07.024.

[9] Christian, J. A., and Lightsey, E. G., "Onboard Image-Processing Algorithm for a Spacecraft Optical Navigation Sensor System," *Journal of Spacecraft and Rockets*, Vol. 49, No. 2, 2012, pp. 337–352. https://doi.org/10.2514/1.A32065.

[10] Christian, J. A., "Optical Navigation Using Planet's Centroid and Apparent Diameter in Image," *Journal of Guidance, Control, and Dynamics*, Vol. 38, No. 2, 2015, pp. 192–204. https://doi.org/10.2514/1.g000872.

[11] Morita, H., Shirakawa, K., Kubota, T., Hashimoto, T., and Kawaguchi, J., "Hayabusa's Real-time Landmark Tracking Navigation for Descents and Touching-Downs," *AIAA/AAS Astrodynamics Specialist Conference and Exhibit*, American Institute of Aeronautics and Astronautics, 2006. https://doi.org/10.2514/6.2006-6537.

[12] Adam, C. D., et al., "Transition from Centroid-Based to Landmark-Based Optical Navigation During OSIRIS-REx Navigation Campaign at Asteroid Bennu," *RPI Space Imaging Workshop*, 2019.

[13] Torre, F., Grey, S., and Vasile, M., "Angles-Only Navigation in the Proximity of a Binary Asteroid System," *Journal of Guidance, Control, and Dynamics*, Vol. 44, No. 1, 2021, pp. 57–74. https://doi.org/10.2514/1.g004355.

[14] Stastny, N. B., and Geller, D. K., "Autonomous Optical Navigation at Jupiter: A Linear Covariance Analysis," *Journal of Spacecraft and Rockets*, Vol. 45, No. 2, 2008, pp. 290–298. https://doi.org/10.2514/1.28451.

[15] Jia, H., Zhu, S., and Cui, P., "Observability-Based Navigation Using Optical and Radiometric Measurements for Asteroid Proximity," *IEEE Transactions on Aerospace and Electronic Systems*, Vol. 56, No. 4, 2020, pp. 2677–2688. https://doi.org/10.1109/TAES.2019.2953947.

[16] Huixin, Y., Xixiang, Y., and Weihua, Z., "State estimation of spacecraft formation near small asteroid," *Proceedings of 2014 IEEE Chinese Guidance, Navigation and Control Conference*, 2014, pp. 55–60. https://doi.org/10.1109/CGNCC.2014.7007219.

[17] Gil-Fernandez, J., and Ortega-Hernando, G., "Autonomous vision-based navigation for proximity operations around binary asteroids," *CEAS Space Journal*, Vol. 10, No. 2, 2018, pp. 287–294.

[18] Takahashi, S., and Scheeres, D. J., "Autonomous Exploration of a Small Near-Earth Asteroid," *Journal of Guidance, Control, and Dynamics*, Vol. 44, No. 4, 2021, pp. 701–718.

[19] Caroselli, E., Belien, F., Falke, A., Curti, F., and Förstner, R., "NEO-MAPP μLander GN&C for Safe Autonomous Landing on Small Solar System Bodies," *AAS GNC Conference*, 2022.

[20] Caroselli, E., Martin, M., Atkinson, K. R., Curti, F., and Förstner, R., "Autonomous lidar-free hazard detection and landing site selection for small bodies descent," *AAS GNC Conference*, 2023. Not yet published.

[21] Caroselli, E., Belien, F., Falke, A., and Curti, F., "Deep learning-based passive hazard detection for asteroid landing in unexplored environment," *AAS GNC Conference*, 2022.

[22] *"Hera Didymos reference model"*, ESA, esa-tecsp-ad-017258 ed., 02 2020. Revision 3.

[23] Kaula, W., *Theory of Satellite Geodesy: Applications of Satellites to Geodesy*, Blaisdell Publishing Company, 1966.

[24] Winkler, T., Kaplinger, B. D., and Wie, B., "Optical Navigation and Fuel-Efficient Orbit Control Around an Irregular-Shaped Asteroid," *AIAA Guidance, Navigation, and Control (GNC) Conference*, American Institute of Aeronautics and Astronautics, 2013. https://doi.org/10.2514/6.2013-5117.

[25] Werner, R. A., and Scheeres, D. J., "Exterior gravitation of a polyhedron derived and compared with harmonic and mascon gravitation representations of asteroid 4769 Castalia," *Celestial Mechanics and Dynamical Astronomy*, Vol. 65, No. 3, 1997. https://doi.org/10.1007/bf00053511.

[26] Nolan, M. C., Magri, C., Howell, E. S., Benner, L. A. M., Giorgini, J. D., Hergenrother, C. W., Hudson, R. S., Lauretta, D. S., Margot, J.-L., Ostro, S. J., and Scheeres, D. J., "Shape Model of Asteroid (101955) Bennu Bundle V1.1," , 2021. https://doi.org/10.26033/33BA-S419.

[27] Gaskell, R., Saito, J., Ishiguro, M., Kubota, T., Hashimoto, T., Hirata, N., Abe, S., Barnouin, O., and Scheeres, D., "Gaskell Itokawa Shape Model V1.0," *NASA Planetary Data System*, 2008.

[28] Simplicio, P. V. M., "Guidance and Control Elements for Improved Access to Space: from Planetary Landers to Reusable Launchers," Ph.D. thesis, 2019. URL https://research-information.bris.ac.uk/en/studentTheses/e2e36630-aa1f-4c9e-84a0-1fc290603520.

[29] Jean, I., Ng, A., and Misra, A. K., "Impact of solar radiation pressure modeling on orbital dynamics in the vicinity of binary asteroids," *Acta Astronautica*, Vol. 165, 2019, pp. 167–183. https://doi.org/https://doi.org/10.1016/j.actaastro.2019.09.003.

[30] Walter, U., *Astronautics*, 3rd ed., Springer International Publishing, Cham, Switzerland, 2019.

[31] Martin, I., Dunstan, M., and Sanchez Gestido, M., "Planetary Surface Image Generation for Testing Future Space Missions with PANGU," *2nd RPI Space Imaging Workshop*, Sensing, Estimation, and Automation Laboratory, United States, 2019.

[32] Oh, S.-M., and Johnson, E., "Relative Motion Estimation for Vision-Based Formation Flight Using Unscented Kalman Filter," *AIAA Guidance, Navigation and Control Conference and Exhibit*, American Institute of Aeronautics and Astronautics, 2007. https://doi.org/10.2514/6.2007-6866.

[33] Otsu, N., "A Threshold Selection Method from Gray-Level Histograms," *IEEE Transactions on Systems, Man, and Cybernetics*, Vol. 9, No. 1, 1979, pp. 62–66. https://doi.org/10.1109/TSMC.1979.4310076.

[34] Montenbruck, O., and Gill, E., *Satellite Orbits*, Springer Berlin Heidelberg, 2000. https://doi.org/10.1007/978-3-642-58351-3.

[35] Bar-Shalom, Y., Li, X.-R., and Kirubarajan, T., *Estimation with Applications to Tracking and Navigation*, John Wiley & Sons, Inc., 2001. https://doi.org/10.1002/0471221279.

[36] *"Hera proximity operations"*, ESA, 5, esa-tecsag-tn-011315 ed., 02 2020. Revision 1.

[37] Fontcuberta, I., "Landing a cubesat on an asteroid's moon," Ph.D. thesis, Politecnico di Milano, 2021.

[38] Hendrycks, D., and Dietterich, T., "Benchmarking Neural Network Robustness to Common Corruptions and Perturbations," , 2019.

[39] Stockman, G., and Shapiro, L. G., *Computer Vision*, Pearson, Upper Saddle River, NJ, 2001.

[40] Pugliatti, M., Franzese, V., and Topputo, F., "Data-Driven Image Processing for Onboard Optical Navigation Around a Binary Asteroid," *Journal of Spacecraft and Rockets*, Vol. 59, No. 3, 2022, pp. 943–959.

[41] Kaluthantrige, A., Feng, J., Gil-Fernández, J., and Pellacani, A., "Centroiding technique using machine learning algorithm for space optical navigation," *3rd IAA Conference in Space Situational Awareness*, 2022, pp. 1–13.